Results in Chemistry 5 (2023) 100699

Contents lists available at ScienceDirect

Results in Chemistry

journal homepage: www.sciencedirect.com/journal/results-in-chemistry

Effective strategies for improved optoelectronic properties of graphitic carbon nitride: A review

Aleena Azhar [a,1], Muhammad Aanish Ali [a,1], Ijaz Ali [b,c], Tae Joo Park [b,*], Muhammad Abdul Basit [a,*]

[a] Department of Materials Science and Engineering, Institute of Space Technology, Islamabad 44000, Pakistan
[b] Department of Materials Science and Chemical Engineering, Hanyang University, Ansan 15588, Republic of Korea
[c] Institute of Materials, Minerals & Mining Engineering, Abbottabad University of Science and Technology, Pakistan

ARTICLE INFO

Keywords:
$g\text{-}C_3N_4$
Nanocomposites
Photocatalysis
Quantum-dots
Synthesis

ABSTRACT

Graphitic carbon nitride ($g\text{-}C_3N_4$) is a promising two-dimensional material having a nanostructured morphology and non-toxic nature that is metal-free and environmentally friendly. Optical, electronic, and chemical sciences are expanded by the many applications of $g\text{-}C_3N_4$. However, $g\text{-}C_3N_4$ offers lower absorbance of solar light, transmitting the higher wavelengths of visible light and the near-infra red and infrared light, restricting its utility for solar light-dependent applications such as photocatalysis, photovoltaics, water splitting, dye degradation, and deterioration of harmful organics. Due to its enhanced thermal, hydrothermal and chemical stability, compelling band gap structure (2.7 eV), and eco-friendliness, $g\text{-}C_3N_4$ has become a powerful substitute for metal and semiconductor-based catalysis. In this review, we highlight the synthesis and modifications of $g\text{-}C_3N_4$ relevant to certain important applications. We also computed certain recent modifications and effective strategies to improve the optoelectronic properties of $g\text{-}C_3N_4$ and thus arrived finally at interesting avenues for future research.

Introduction

Environmental problems and energy concerns have accompanied global economic expansion [1–3]. Photocatalytic reactions are promising candidates to address these issues [3–5]. Compared to conventional biological and chemical methods, semiconductor-based photocatalytic reactions are eco-friendly and productive [6–9]. In addition applications such as hydrogen evolution [8,10–12], organic dye degradation [13–17], and CO_2 reduction [18,19] have been addressed using semiconductors like titania (TiO_2) [20], boron nitride (BN) [21], phosphorus (P) [22], zinc oxide (ZnO) [23], and bismuth tungstate (Bi_2WO_6) [24]. Wang et al. [25] revealed that $g\text{-}C_3N_4$ showed exceptional performance in photocatalytic water splitting upon exposure to sunlight. By the virtue of its hydrothermal balance, advantageous energy gap of 2.7 eV and adequate sunlight-driven photochemical performance [26,27], $g\text{-}C_3N_4$ is a potential material to address global energy issues [28–30]. Certain limitations that impede the practical use of neat $g\text{-}C_3N_4$ include its low absorption of sunlight [31], higher risk for detrimental charge recombination [32], limited specific area [33–35] and low efficiency [36]. To overcome such issues associated with $g\text{-}C_3N_4$, certain effective strategies can be employed like doping [37–40], applying a passivation layer [38,41,42], depositing metals on its surface [42], tuning its size and morphology [43–48], introducing heterojunctions [49–53], and introducing nanocomposites using quantum dots [54–57].

Quantum dots (QDs) are quite appealing due to their efficiency in sunlight-dependent applications [58–60]. Its low specific surface area, enhanced deterioration of charges and low optical density give $g\text{-}C_3N_4$ low photoactivity [50]. Certain strategies have been employed to improve the absorbance properties of the bare $g\text{-}C_3N_4$ including metal doping using iron (Fe) [61], silver (Ag) [49], and certain non-metals like sulfur (S) [62] and boron (B) [16]. Certain materials have been aligned with the band gap of $g\text{-}C_3N_4$ at impurity concentration levels to intensify the absorbance of solar light by band gap engineering. Besides doping, nanocomposite formation is another effective strategy to improve the sunlight absorbance of the material. Several other modifications used to

* Corresponding authors.
E-mail addresses: tjp@hanyang.ac.kr (T.J. Park), ab_saim@hotmail.com, m.abdulbasit@mail.ist.edu.pk (M. Abdul Basit).
[1] Both authors contributed equally as first author.

https://doi.org/10.1016/j.rechem.2022.100699
Received 25 October 2022; Accepted 29 November 2022
Available online 1 December 2022

increase the optoelectronic performance include defect control, porosity, morphological modifications and enhanced surface areas for absorption based on hollow spherical structures, nanorods, and 3D structures [63]. To ensure the increased absorption of solar light by modification of g-C_3N_4, it is important to ensure the band gap alignment of the g-C_3N_4 and the introduced semiconductor material for effective transport of the charges [64–66].

CQDs have recently been coupled with g-C_3N_4 and were extensively studied for water splitting and other applications [67]. Certain modifications of g-C_3N_4 are depicted in Scheme 1. This review summarizes contemporary research regarding the photocatalytic performance of g-C_3N_4 and its various modifications. We describe recent design approaches based on g-C_3N_4 applications and effective strategies for employing them.

Graphitic carbon nitride

Carbon nitrides (C_3N_4) consist of carbon and nitrogen elements in the structure of long-chain molecules. Such materials can be derived by replacing carbon or hydrogen (due to unfinished polymerization) with nitrogen atoms in existing structures [33]. Unlike the other carbon-based materials, g-C_3N_4 has some distinct qualities thus making it a suitable yet compatible substitute for carbon in recent applications [68].

Properties of g-C_3N_4

g-C_3N_4 was popularized by Liebig when Berzelius synthesized a linear long-chain compound "melon" in 1834 [69]. However, its insolubility, chemical resistivity, hydrothermal stability, and photostability made it difficult to study until recently [70]. Structurally, g-C_3N_4 consists of C and N with a π-conjugated system. Modernistic methods uncovered the unique attributes of g-C_3N_4, like its extraordinarily stable form of carbon, unique surface properties, photocatalytic behavior, and organic dye degradation activity [29]. Certain small amounts of hydrogen atoms are also present due to abridged condensation polymerization, leading to defects on the surface. Surprisingly, these surface defects play a key role in the resonance of the electrons and make g-C_3N_4 as a Lewis-base suitable for catalysis applications.

Advantages of g-C_3N_4

Owing to the impressive property profile of g-C_3N_4 such as an *n*-type semiconductor, abundant in nature, band gap of 2.7 eV, and appealing electronic structure, it is one of the best candidates to be used in photocatalytic applications, especially water purification assisted by visible light. It contains carbon and nitrogen and some traces of hydrogen which are earth-abundant elements. Unlike graphene and other similar structures, it has a semiconductor nature which differentiates it from others, thus making it suitable for removing organic pollutants from water [71–73]. Moreover, it has optical absorbance at 450 nm and hence exhibits yellow color [74–76]. Unlike the other carbon-based polymeric entities, g-C_3N_4 is resistant to higher temperatures (like 600 °C) making it a suitable candidate to be used at elevated temperatures. Furthermore, the material can be used in heterogeneous reactions due to its resistance to solvents even in the presence of acidic or alkaline media. Thus g-C_3N_4 proved itself to be capable of catalyzing certain chemical and photochemical reactions like photocatalytic dye degradation, photocatalytic water splitting, CO_2 bracing, redox reactions, and therapeutic and antimicrobial applications [77].

Drawbacks of g-C_3N_4

Each material comes with its own set of property profiles which includes both the pros and cons. Likewise, g-C_3N_4 also has some drawbacks which limit its use in photocatalytic applications such as cleaning water. Some of the major disadvantages include but are not limited to (i) photoexcited electron-hole pair recombination [78], (ii) low surface area [79], (iii) low quantum yield (QY) [80], and (iv) below average visible light absorption [81]. In addition to these drawbacks, another limiting factor that hinders its use is the wastage caused by centrifugation or filtration process. This is because g-C_3N_4 is quite difficult to be removed or completely separate from the solution mixture. A lot of time, energy, and resources are wasted in such processes.

Synthesis of g-C_3N_4

g-C_3N_4 is frequently prepared by thermal etching, and bulk material can be prepared by this approach followed by size reduction to smaller particles. The importance of this technique lies in the fact that various morphological assemblies can be produced in this way including dots, nanosheets, and bulk material. The "top-down" synthetic method is performed at high-temperature, i.e., 825–950 °C. To make nanosheets, higher temperatures can be used to reduce the material size, but this may promote thermal corrosion [82]. g-C_3N_4 can be prepared by the thermal or mechanical descaling of bulk material and also by the scale-up of precursors [83]. g-C_3N_4 synthesis dates back to 2013 when the

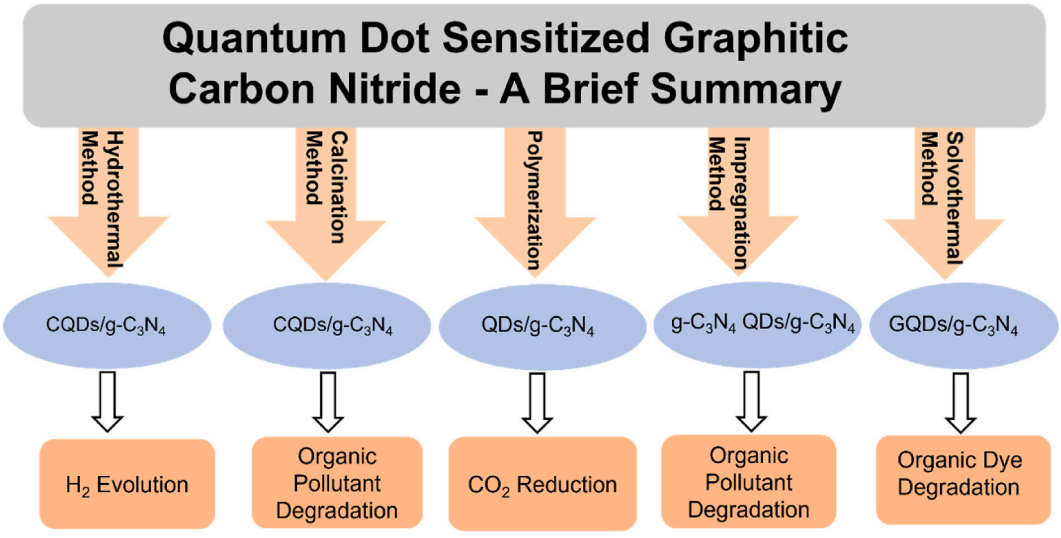

Scheme 1. A brief summary of quantum-dot sensitized g-C_3N_4.

sodium salt derivative of citric acid and urea molecules were thermally catalyzed to produce larger polymeric g-C_3N_4 materials [62]. Certain methods and strategies have been evaluated here for the synthesis of g-C_3N_4 as indicated by Scheme 2.

Chemical method

Thermodynamic and kinetics are critical challenges in the manufacturing and design of single-bonded polymeric structured g-C_3N_4. While looking for the chemical routes to design such material, certain C and N rich compounds like heptazine and triazine were considered. But certain drawbacks hinder their performance including instability, lack of availability, and their dynamite-like nature. These make the design of the material a bit less feasible, and another issue was the thermodynamic feasibility [84,85].

After passing the synthesis challenge, this material proved itself to be an exceptionally good catalyst due to the presence of the defects left as products of the unfinished polymerization reaction. Such defects are required, and the most common method to acquire such structures in g-C_3N_4 is the condensation polymerization reaction using the precursor and intermediates of dicyandiamide and melamine heated to 550 °C [82].

Temperature treatment plays an important role during synthesis as reducing the temperature provides a high surface area, which is an important factor for the applications of g-C_3N_4. However, synthetic approaches to achieve defects in g-C_3N_4 for various applications could be problematic due to the cost, availability, insolubility, and explosivity of the cyanimide [86,87]. Fig. 1 depicts the synthesis of two-dimensional g-C_3N_4 by calcination and the hydrothermal method to achieve high surface area and shows then the effect of altering the operating temperatures on the synthesis, morphology, and crystal structure. Paul et al. provided a schematic for plausible intermediates of g-C_3N_4 during synthesis at different temperatures as depicted in Fig. 1a [88]. The direct calcination method can be used to obtain varying thicknesses of g-C_3N_4 nanosheets. A schematic illustration of different steps for the fabrication of these nanosheets is shown in Fig. 1b as reported by Hong et al. [89]. Analysis of X-ray diffraction (XRD) patterns in Fig. 1c shows that an increase in calcination temperature causes the peak (0 0 2) to shift towards a higher angle (27.3° to 27.9°), which indicates a decrease in the interlayer spacing from 0.328 to 0.319 nm. Hence, an increase in calcination temperature can improve the interlayer stacking order of g-C_3N_4. However, a denser and more compact structure was achieved if it was heated above 550 °C. XRD patterns also showed that the (0 0 2) peak became narrow and intense with increasing temperature. This indicates that an increase in temperature results in increased crystallinity of g-C_3N_4. Moreover, the synthesis of urea-derived g-C_3N_4 occurs above 450 °C. However, excessive heating can result in the decomposition of CN polymer. Scanning electron microscope (SEM) images showed that g-C_3N_4 calcined at 450 °C (Fig. 1d) and 500 °C (Fig. 1e) consists of lumps. g-C_3N_4 calcined at 650 °C (Fig. 1f) resulted in the contraction of layered flakes of g-C_3N_4, which may be due to a decrease in surface area at temperatures above 550 °C. A stacked-layer morphology can be observed from transmission electron microscope (TEM) images in Fig. 1g for a sample of g-C_3N_4 calcined at 550 °C. Miller et al. prepared several g-C_3N_4 compounds from a 1:1 mixture of DCDA and melamine heated above 550 °C to 650 °C in a nitrogen atmosphere [90]. The resulting increase in temperature caused an increase in C:N ratio and a decrease in H:C ratio due to the loss of NH_3 due to condensation reaction. The results can be seen in Fig. 1h. The g-C_3N_4 made at 550 °C showed enhanced absorption and photocatalytic activity due to having highest molecular weight, complete polymerization, and broad surface area [88–90].

Polymerization synthesis

The problems encountered above resulted in the search for another chemical species with higher aqueous solubility, reduced cost, better availability, and eco-friendly nature resulting in the use of guanidine hydrochloride (GndCl) [87]. The direct condensation operation supported thermally at 550 °C for a longer time (three hours) can be employed to generate defects in g-C_3N_4. GndCl was employed in the same scheme used for cyanimide, leading to a better mechanism with intermediate steps of conversion of melamine to melem and then a polymeric structure with g-C_3N_4 as a product. Certain problems with the method also arise like a lower surface area (~10 m^2/g). Surface area is one of the factors controlling the absorbance of the energy by the material as well as its activation and photocatalytic performance. So, this material would be challenging to use in heterogeneous catalysis [91].

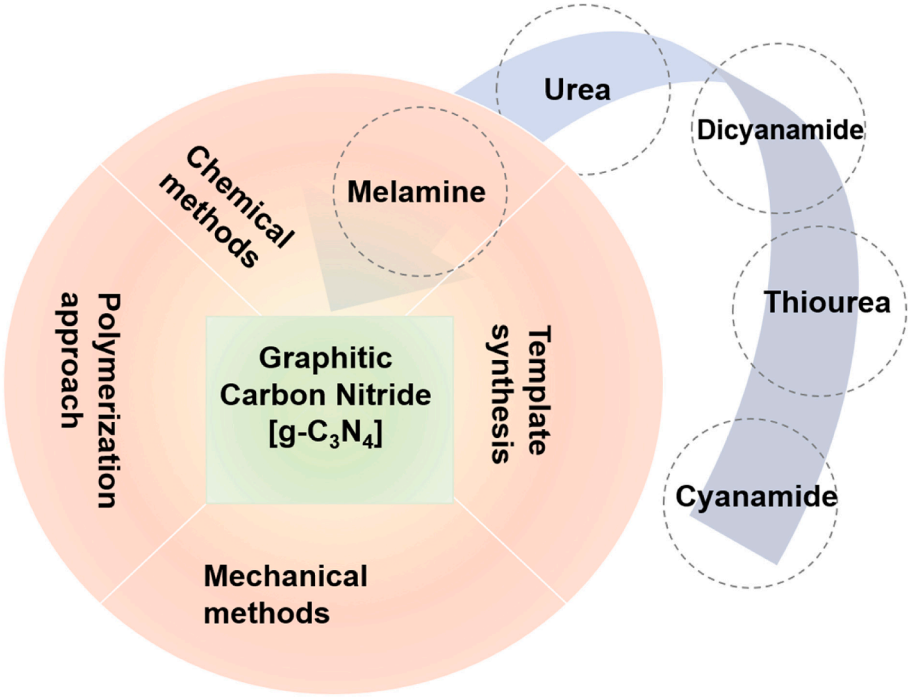

Scheme 2. Materials and methods for preparation of g-C_3N_4.

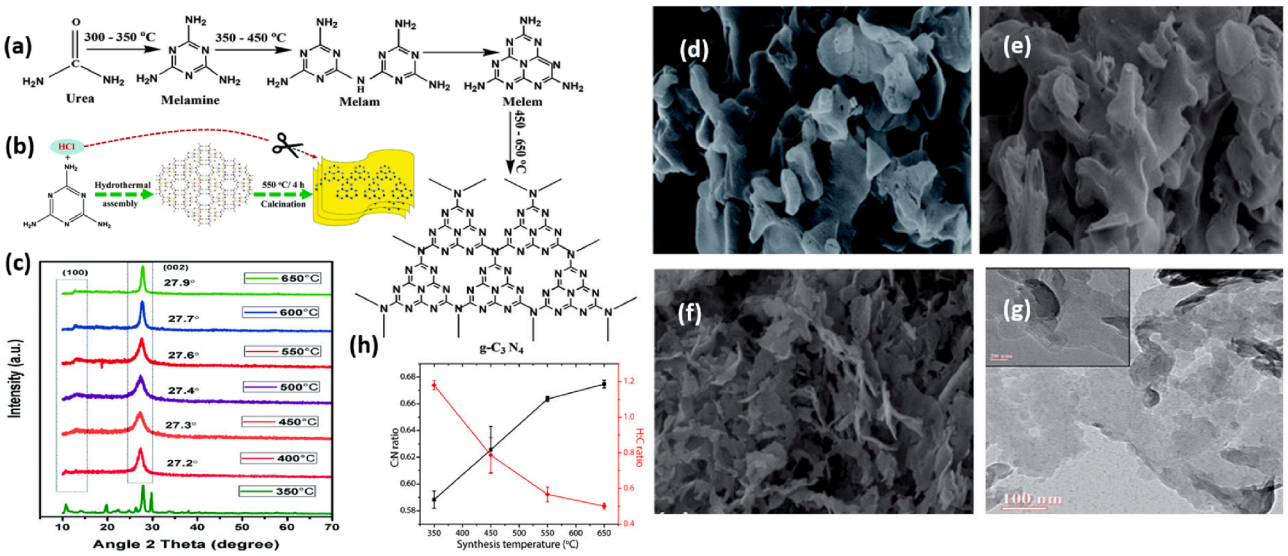

Fig. 1. (a) Schematic representation of the synthesis of g-C_3N_4. (Reprinted with permission from Ref. [88] Copyright 2019 RSC). (b) Representation of adjustment of various thicknesses of g-C_3N_4 sheets by chemical exfoliation. (Reprinted with permission from Ref. [89] Copyright 2017 RSC). (c) XRD patterns of g-C_3N_4 made at different temperatures. SEM images of g-C_3N_4 prepared at (d) 450 °C, (e) 500 °C, (f) 650 °C. (g) TEM micrograph of prepared g-C_3N_4 at 550 °C. (Reprinted with permission from Ref. [88] Copyright 2019 RSC). (h) Atomic ratios of C:N and H:C synthesized at various temperatures (350–650 °C). (Reprinted with permission from Ref. [90] Copyright 2017 RSC).

Bulk g-C_3N_4 is a 2D covalent structure resulting after heating melamine (thermal annealing) to around 600 °C for about 90 min in the presence of air. It is characterized by the three-folded symmetric architecture of tris-s-triazine, which is connected via an in-plane tertiary amine. However, this bulk g-C_3N_4 has few catalytic sites for organic pollutants. Hence, liquid-phase exfoliation is performed in a suitable solvent such as IPA or water. Vacuum filtration is then performed to obtain membranes as depicted schematically in Fig. 2a. Zhou et al. used different IPA volume ratios and employed UV–vis spectroscopy (Fig. 2b and 2c) to achieve a yield of 35 % [92]. Their result is in strong agreement with Khan et al. [93]. We note here that the 90 % yield claimed by Lin et al. [94] does not agree with the results of Zhou et al. TEM images reported by Wang et al. [95] show the morphological nature of bulk g-C_3N_4 (Fig. 2d) and nanosheets of g-C_3N_4 (Fig. 2e). However, Wang et al. claimed to have employed thermal oxidation methods to etch bulk g-C_3N_4 to nanosheets. A widely used Hummers method was not employed in their study as this is suitable for making nanosheets on a larger scale, not a small scale.

Reactive areas of about 97 m^2/g can be achieved in g-C_3N_4 by employing the direct polymerization method referred to as the

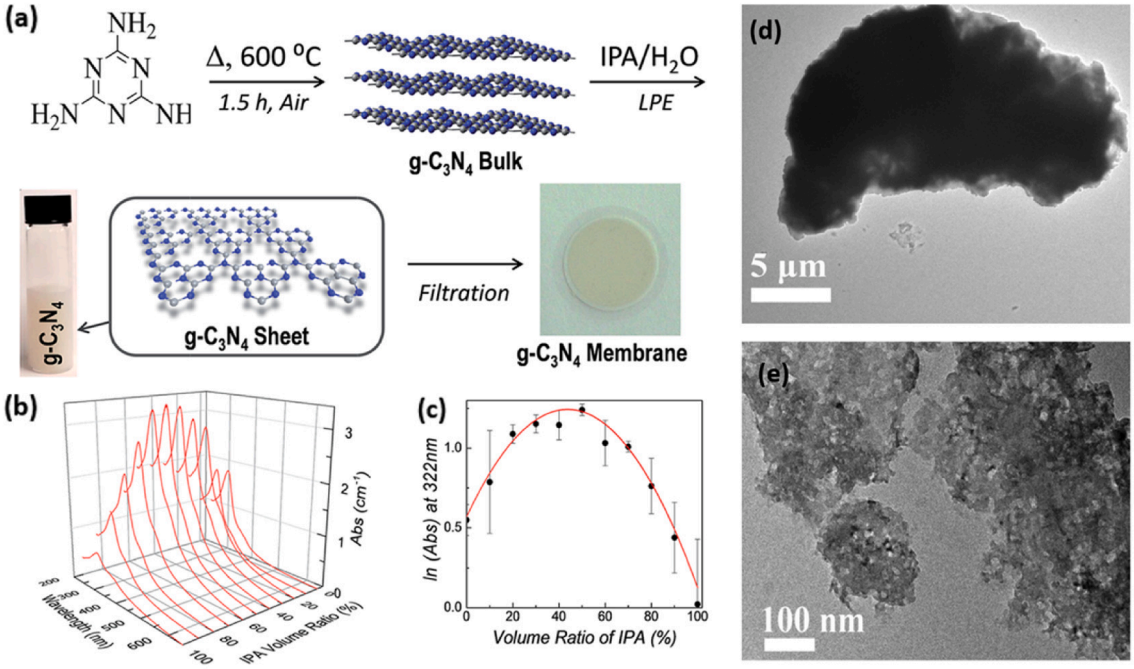

Fig. 2. (a) Schematic illustration of the synthesis of g-C_3N_4 by melamine and then exfoliation in IPA/H_2O. (b) Ultraviolet spectrum of diluted g-C_3N_4. (c) Concentration ratio of g-C_3N_4 in IPA/H_2O. (Reprinted with permission from Ref. [92] Copyright 2016 RSC). (d) TEM analysis of nanosheets of g-C_3N_4. (e) TEM analysis of bulk g-C_3N_4. (Reprinted with permission from Ref. [95] Copyright 2014 RSC).

polycondensation approach, which does not require a template. Zou et al. showed lower temperature synthesis (300 °C) of the g-C_3N_4 from urea [96,97]. Certain hydroxide (–OH) modified mesoporous TiO_2 entities were also reported. Low-temperature attack of the –OH group on the carbonyl unit of urea yields titanol, which further attacks the carbonyl crowds to obtain the intermediate amine group (–NH_2) groups and ultimately discharges the g-C_3N_4 [98].

Impregnation or template synthesis

The surface area problem was overcome using SBA-15 to make g-C_3N_4 which achieved better performance in catalysis [25]. The longer g-C_3N_4 polymer chain structure can be employed as a film or a coating on another scaffold to increase the surface area and provide better performance. Wang et al. employed an impregnation method to achieve surface areas from 8 to 506 m^2/g, resulting in a photocatalytic activity increase from 0 Hz to 15 Hz. The material used was a nanocomposite of g-C_3N_4 containing iron in the structure deposited on SBA-15.

A powerful method for achieving high surface area involves introducing porosity in the material itself despite using another support. The template method (Ludox HS40 Silica) can be employed to achieve such porous graphitic materials with improved properties. Enhanced attributes can be achieved by making a composite and introducing porosity into it. Porosity improves the surface area to volume. The area of the material available for reaction can also be controlled based on the amount of patterning template used [77]. Zheng et al. proposed a synthesis scheme for g-C_3N_4 via a nano-casting method [99]. They chose chiral mesoporous silica (CMS) as a sacrificial template since its unique helical hexagonal rod-shaped morphology allows for assembly of twisted nano-architectures by directing the assembly of building blocks [100]. Cyanimide (CY) precursor is infiltrated into this template for the preparation of helical nanorods of g-C_3N_4 (HR-CN). The resulting structure of HR-CN along with parameters for each step of synthesis are schematically illustrated in Fig. 3a. Ovcharov et al. proposed the hard template synthesis of g-C_3N_4 [100]. They used porous C_3N_4 (PCNs) of various morphologies obtained from bulk and hard template pyrolysis of melamine. These PCNs were found to be p-type semiconductors that showed catalytic activity towards photoreduction of CO_2 with H_2O (water vapor). The PCNs obtained in MCF showed greater bandgaps, higher photocatalytic activity, and a sponge-shaped morphology. The proposed scheme is shown in Fig. 3 b. In another study by Hwang et al., SEM and TEM results were obtained for g-C_3N_4 samples formed after etching of a silica template [101]. Uniform spherical pores of around 260 nm can be seen in the images of both TEM and SEM as shown in Fig. 3c and3d. However, small pores of around 60 nm (connected spherical pores) are visible in SEM micrographs. These contact points play a significant role in the removal of silica spheres in the template using an HF solution. The original silica spheres were about 290 nm in diameter and the observed pore sizes were 260 nm. This indicates roughly 10 % shrinkage due to the polymerization process. TEM images of Fe-g-C_3N_4 showed the absence of aggregated species and 2D hexagonal structure as shown in Fig. 3e. Elemental mapping results further confirmed the homogeneous coating on SBA-15 of Fe-g-C_3N_4. Wavelength dependent results also confirmed the enhanced activity of Fe-g-C_3N_4/SBA-15 based on the UV/vis diffuse reflectance spectrum as shown in Fig. 3f.

Charge transfer dynamics in Z-scheme heterojunctions

Z-scheme was introduced in the year 1979 by Bard taking inspiration from photosynthesis process [102]. For understanding these semiconductor heterojunctions, we have given schematic illustrations for types of Z-scheme heterojunctions in Scheme 3, regarding the photocatalytic action of these schemes and how they differentiate from one another. As shown in Scheme 3 **(a)**, the traditional Z-scheme is constructed by combining two different semiconductors (SC-I and SC-II) with a redox mediator which helps in transferring charges from one semiconductor to another. Upon irradiation by visible light, electrons in SC-II are photoexcited in CB and are accepted by electron acceptor (A). Subsequently, (A) is reduced to become an electron donor (D). Thereafter, holes present in SC-I oxidize the (D) back to (A) and hence the cycle of electron transfer continues from one to another semiconductor. The traditional Z-scheme efficiently facilitates charge transfer and separation simultaneously. It is pertinent to mention here that this type of Z-scheme does not have any disadvantages associated with it. However, the use of these kinds of heterojunctions is only limited to liquid state systems due to the presence of this redox mediator solely in the liquid

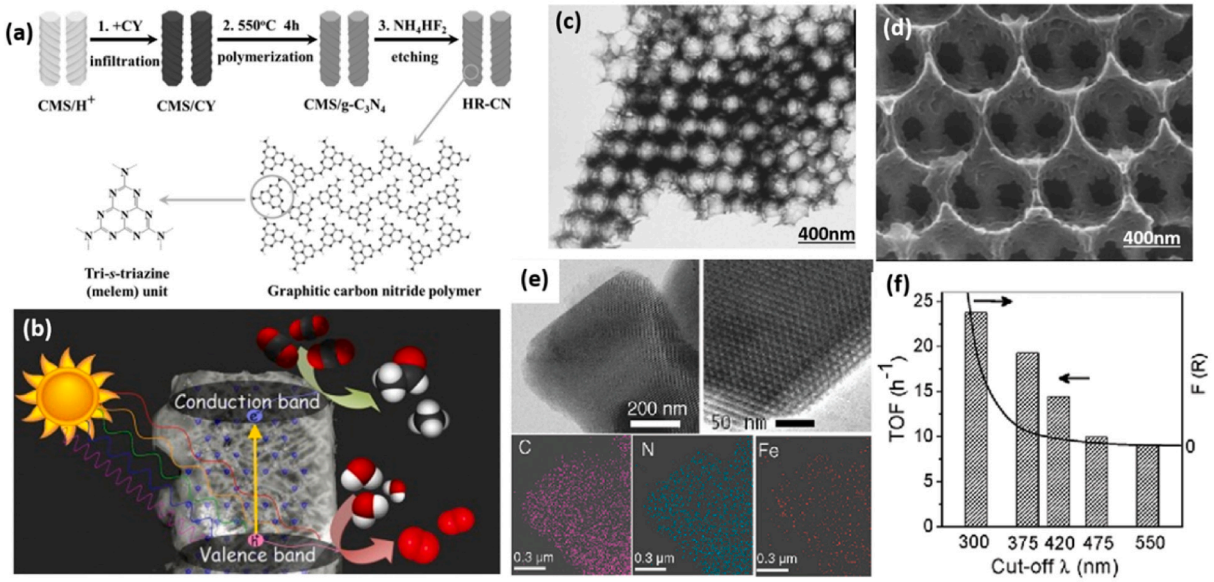

Fig. 3. (a) Schematic illustration of the synthesis of g-C_3N_4. (Reprinted with permission from Ref. [99] Copyright 2014 Wiley). (b) Illustration of the hard template synthesis through (SBA-15 and MCF) pyrolysis of melamine. (Reprinted with permission from Ref. [100] Copyright 2015 Elsevier). (c) TEM image of the g-C_3N_4 synthesized by the template method. (d) SEM image of the g-C_3N_4 synthesized by the template method. (Reprinted with permission from Ref. [101] Copyright 2007 Elsevier). (e) TEM images along with elemental mapping of g-C_3N_4 supported on SBA-15. (f) Phenol production rate dependence on the g-C_3N_4 composite. (Reprinted with permission from Ref. [91] Copyright 2009 ACS).

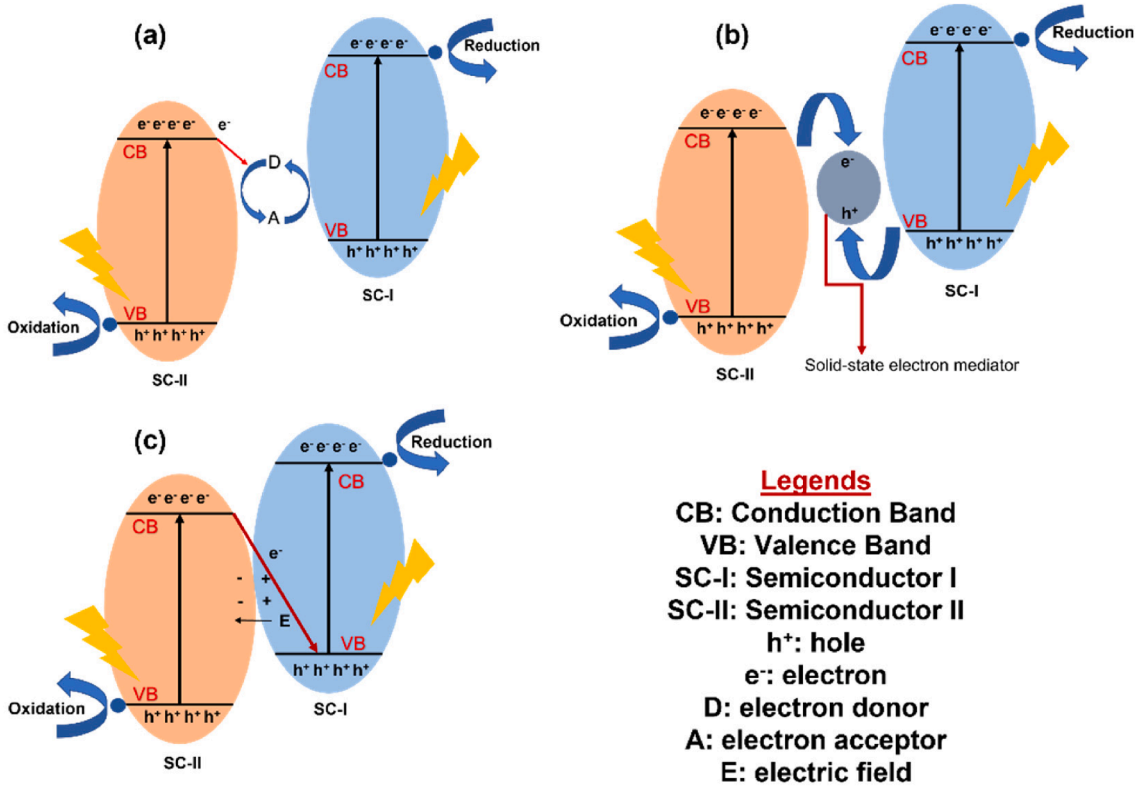

Scheme 3. Schematic illustrations of (a) Traditional Z-scheme, (b) Solid-state Z-scheme and (c) Direct Z-scheme.

phase [103]. The other type of Z-scheme is called the solid-state Z-scheme which is shown in Scheme 3 **(b)**. The difference between traditional and solid-state Z-scheme is the presence of a solid-state electron mediator in this case. Moreover, there are some advantages associated with solid-state Z-scheme over the traditional one. For instance, it can be used for both liquids and gaseous phases, the charge transfer capability is sufficiently enhanced when the difference in electrical resistances of two semiconductors is increased, and the absence of reverse reaction as with traditional Z-scheme and the renewable system due to solid-state electron mediator. There are, however, many drawbacks associated with solid-state Z-scheme such as high chances for photocorrosion, and interference of light which in turn affects the absorbance of semiconductors and expensive solid mediators [104]. But perhaps the most used and known scheme which we also have thoroughly discussed in this review is direct Z-scheme of which schematic illustration can be seen in Scheme 3 **(c)**. There is an absence of both redox and electron mediators since the two semiconductors are directly in contact with one another. As a result, the transmission distance is reduced significantly. The presence of an electric field (denoted by E in the schematic) facilitates charge transfer. Band edge potentials and work functions of semiconductors dictate the charge separation. Under the influence of visible light, the photoexcited electrons from CB of SC-II migrate towards VB of SC-I, thereby combining with its holes and hence resulting in production of spatially separated charge carriers which have better capability for surface reactions. It is important to note here that certain parameters such as contact, morphology, and textural properties of both semiconductors need to be carefully managed for effective charge transmission to surface [105].

Certain other methods (Table 1) can also be used to obtain different morphologies and designs of the material.

Strategic applications of g-C_3N_4 and its nanocomposites

Photocatalytic water splitting

As compared to conventional fuels, hydrogen gas (H_2) is predicted to be around 90 % of all energy sources by the year 2080 [164]. Around 44.5 million tons of this gas are produced per year throughout the world [64]. Steps must be taken to explore production and usage in almost all fields and applications like energy conservation and transportation [165]. Eco-friendly, green, and economical approaches are under consideration for hydrogen evolution [165,166]. Currently, the energy issues focus on a solar light-driven catalytic approach for hydrogen generation reaction and water splitting using solar energy as a driving force [167,168].

Remarkable work was accomplished by some leading automotive companies since the late twentieth century [169], yet challenges remain in the photocatalytic materials for splitting water and generating hydrogen fuel [170,171]. Nanomaterial-based photocatalysts are mostly oxide materials due to their higher stability [61], but their higher band gap energy requirement involves the ultraviolet portion of the solar light, which is a small portion of the whole spectrum. This results in lower absorbance. So, it is important to utilize and absorb the major part of the solar spectrum (e.g., the visible region), leading to a better, stable, industrial, economical, and eco-friendly energy source. After absorbing the sunlight, the photogeneration of electrons and holes takes place, leading to a water splitting reaction. Certain important considerations involve the control of toxicity, photocatalyst stability and detrimental charge recombination through various strategies. The band gap is an important factor for the performance as the hydrogen generation reaction requires an energy gap higher than 1.23 eV. Moreover, the relative positions of the conduction and the valence bands must be carefully tailored to check the charge carrier dynamics and make the reaction feasible thermodynamically [172].

g-C_3N_4 is a promising candidate for solar energy-based reactions

Table 1
Summary of various nanocomposites and hybrid materials of g-C_3N_4 for improved optoelectronic performance.

Material	Method	Application	Novelty	Activity	Reference
Sg- C_3N_4	Simple sulfonation	Biodiesel	Biodiesel	Easy accessibility, low cost and stability	[106]
SNGQDs	Spin coat	Water splitting	Photocurrent enhancement of ~ 4.5x	Enhanced photocatalysis	[107]
g-C_3N_4-NS/CDs/ BiOI	Thermal, precipitation method	Photocatalytic dye degradation	Deposition of CdS on g-C_3N_4	Enhanced absorption and charge separation	[108]
Ug-C_3N_4-Ps	Ball milling	H_2 evolution	greater than13.7-fold than Bulk	Improved electron transfer ability and aligned energy levels	[109]
g-C_3N_4-HC	Calcination, salt intercalation	Photocatalytic activity	Scalable synthesis	Fewer structural defects	[110]
TiO_2 deposited with MoS_2/g-C_3N_4	Hydrothermal method and impregnation approach	Dye degradation	Enhanced charge separation performance using PL analysis	Extended absorbance	[111]
$MnIn_2S_4$/g-C_3N_4	Hydrothermal method	Degradation of waste and hydrogen generation	Smart structure design	CH degradation and H_2 evolution	[112]
g-C_3N_4/CeO_2	Facile calcination	H_2, degradation of organic dye	Competent and direct Z-scheme	More active than P25	[113]
$CoTiO_3$/g-C_3N_4	Precipitation method	H_2 evolution	Direct Z-scheme	Boost the photocatalysis	[114]
WO_3/g-C_3N_4	Simple calcination	H_2 evolution	Composite	Efficient charge separation	[115]
Au/g-C_3N_4	Deposition precipitation strategy	H_2 evolution	Mechanism	High photocatalytic activity	[116]
Pt/g-C_3N_4	Thermal/impregnation method	H_2 evolution	Higher band energy provides higher driving force for reaction	Increased water splitting	[117]
Rh/g-C_3N_4	Hydrolysis	H_2 evolution	Enhanced photocatalysis	Efficient charge carrier dynamics require more Rh particles	[118]
$Ni(OH)_2$-g-C_3N_4	Precipitation	H_2 evolution	Economical hydroxide counterfeiting the noble metals	Efficient co-catalyst	[119]
Ag/g-C_3N_4	Hydrolysis method	H_2 evolution	The rate of photocatalysis increased	Up to 4.8 times higher rate is observed as compared to the 3 wt% composite	[120]
Au/g-C_3N_4	Chemical reduction	H_2 evolution	Photosensitizer	The rate of H_2 generation is enhanced	[121]
1 T-MoS_2 QDs	Hydrothermal method	Photocatalytic H_2 evolution	Enhanced photocatalysis of the hybrid	High HER activity under visible light energy	[122]
Cobalt-Melamine	Condensation reaction	H_2 release reaction	33.1/13.2 Modified surface area/ pristine area/pristine	3-fold enhanced photocatalytic activity	[123]
P/ g-C_3N_4	Co-polycondensation	H_2 evolution	Nano-flowers with mesoporosity	Activity enhancement (9.3 times) increased surface area over pristine	[124]
P/ g-C_3N_4	Co-polycondensation, thermal exfoliation strategies	H_2 evolution	Doped and porous nanosheets	14.8-fold modified surface area/ pristine	[125]
P-doped g-C_3N_4	Co-polycondensation	H_2 evolution	P doping in g-C_3N_4	Absorbance decreased; charge separation increased	[126]
P- Melamine (CN)	Hydrothermal treatment, self-assembly	H_2 evolution	The layered stacked tubular structure	Improved absorbance and enhanced charge separation, increased HER rate (67 μmol h^{-1})	[127]
$C_3N_4 - xS_x$	Heating-treated in H_2S	H_2 evolution	Homogeneous substitution of S for N, concomitant quantum confinement	High H_2 evolution	[128]
Sulfur-doped g-C_3N_4	Co-polycondensation	H_2 evolution	S/ g-C_3N_4	H_2 evolution rate increased 6-fold	[129]
Sulfur-doped g-C_3N_4	Polycondensation	H_2 evolution	Doping with sulfur	CNS 30 times more active	[130]
O/ g-C_3N_4	Hydrothermal	H_2 evolution	Facile H_2O_2 hydrothermal approach	Enhanced visible-light photoactivity	[131]
O/g-C_3N_4	Calcination	H_2 evolution	Synergetic interaction of porous network and O-doping	Upgraded HER rate	[132]
O-doped g-C_3N_4 PUOCNs	Chemical oxidation	H_2 evolution	Permeable ultrathin nanosheets	H_2 evolution rate amplified ~ (5.2 X)	[133]
Holey Structure g-C_3N_4-O	Light oxidation	H_2 evolution	Thin sheets with O doped structure	Higher H_2 evolution and dye degradation	[134]
B/g-C_3N_4	Co-polycondensation	H_2 evolution	Simultaneous modifications of the textural, surface, electronic structures of rigid CN	Improved absorbance and enhanced charge separation	[135]
g-C_3N_4	Co-polycondensation	H_2 evolution	Photocatalysis	Improved light absorbance	[136]
Iodine functionalized g-C_3N_4	Co-condensation	H_2 evolution	Iodine modified g-C_3N_4	Increased photocatalytic activities	[137]
I-g-C_3N_4-Ss	Ball milling	H_2 evolution	Doped nanosheets synthesized by facile strategy	High H_2 production rate	[138]
Bromine doped g-C_3N_4	Co-condensation	H_2 evolution	Deposition of cobalt oxide	Higher H_2 evolution rates, with high stability	[139]
O-doped (C_3N_4) nanosheets	Up-conversion	H_2 evolution	Extended lifetime of photogenerated electrons	H_2 generation accelerated under ultraviolet and infrared light	[140]
CV-g-C_3N_4	Thermal treatment	Photocatalysis	Fabrication with carbon vacancy	Enhanced photocatalytic activity	[141]
H g-C_3N_4	Thermal treatment	H_2 evolution	Hole-filled graphitic(2D) structure, porous	~20 times higher photocatalytic hydrogen production	[142]
Carbon sphere loaded on g-C_3N_4	Hydrothermal treatment	Degradation of water contaminants, dye degradation	Photocatalysis based on carbon nanosphere morphology	Enhanced photocatalysis	[143]
g-C_3N_4	Facile synthesis		Cost-effective strategy	Boosted photocatalysis	[144]

(*continued on next page*)

Table 1 (*continued*)

Material	Method	Application	Novelty	Activity	Reference
		Generate hydrogen and decontaminate wastewater			
Porous g-C_3N_4	Acidic cutting and hydrothermal process	H_2 evolution	Reduced aggregation	Intensified HER rate under visible light	[145]
g-C_3N_4 Nanosheets/ CeO_2/Fe_3O_4	Facile co-precipitation routes	Potential for advanced wastewater treatment	Ternary composite nanosheets	Efficacious charge separation, higher photocatalysis	[146]
Tubular g-C_3N_4	Chemical route	ORR	Propriety to be used for fuel cells	Morphology dependent performance	[147]
C_3N_4	Thermal condensation	H_2 evolution	Conciliatory donor for Hydrogen generation studies	Artificial conjugated polymer semiconductors energy transducers	[25]
g-C_3N_4, g-C_3N_4M, and Fe-g-C_3N_4	Hydrothermal method	Photocatalysis	Ternary hybrid structure	Reinforced photocatalysis for RhB and Cr (VI)	[148]
g-C_3N_4 nano-meshes	Ab initio simulation	H_2 evolution	Aggregation of 2D g-C_3N_4 avoided by NVG	Charge redistribution, interfacial charge separation	[149]
g-C_3N_4/MoS_2	Facile and scalable one-step method	Mesopores, effective heterojunction	Enhanced photocatalysis	3-fold enhanced photocatalytic activity	[150]
ZnO/CuS	Precipitation method, thermal treatment	H_2 evolution	Z-scheme system	Improved hydrogen generation	[151]
Y- g-C_3N_4, C-g-C_3N_4	Facile and environmental-friendly method	Photocatalysis	Defect engineering	Improved hydrogen generation (5 times)	[152]
Nanoporous g-C_3N_4	Artificial photocatalysis	Fuel cells, photocatalysis, ORR	Artificial photocatalysis for hydrogen production	Photocatalysis, heterogeneous catalysis	[153]
g-C_3N_4	Template synthesis	Synthesis Mechanism	Tunable porosity	Synthesis-based	[154]
g-C_3N_4	Thermal treatment	Dye degradation, photocatalysis	Layered structure	Increased vis light active photocatalysis carbon/ TiO_2	[33]
g-C_3N_4–Ag_3PO_4	Precipitation method	Photocatalysis	Economical approach	Good photocatalysis	[155]
CDs/g-C_3N_4	Hydrothermal	H_2 evolution	A facile hydrothermal approach	Enhanced efficiency	[156]
g-C_3N_4 NSs/CQDs	Hydrothermal	H_2 evolution	Rapeseed flower bee pollen coupled with U g-C_3N_4	Efficiency 88.1 μmol h^{-1}	[157]
CQD-implanted g-C_3N_4 NT	Polymerization	H_2 evolution	CQDs into the surface layer	Enhanced efficiency	[158]
CDs with g-C_3N_4 hybrids	Polymerization	H_2 evolution	Novel hybrid	Efficiency 2.34 mmol $g^{-1}h^{-1}$	[159]
CDs and CdS-QDs modified g-C_3N_4	Solvothermal method	H_2 evolution	Hybrid and structure	Enhanced efficiency	[160]
CDs/g-C_3N_4/TiO_2	Impregnation precipitation	H_2 evolution	Ternary layered nanosheets	Enhanced efficiency	[161]
g-C_3N_4/BCNQDs	Molten salt	H_2 evolution	g-C3N4 heterojunction	Enhanced efficiency	[162]
Ag QDs/g-C_3N_4	Hydrothermal approach	H_2 evolution	CNS NIR-response photocatalysts	Enhanced efficiency	[163]

involving the hydrogen evolution reaction. Even so, its higher band gap energy offers absorbance only in a limited region of sunlight, and a faster detrimental charge recombination factor limits its performance. Certain reduction co-catalysts and metals like platinum (Pt) can be utilized to overcome these problems. Such materials offer higher absorbance and lower charge annihilation resulting in higher performance in the water-splitting reaction. Certain quantum dots and other sulfides (S^{2-}) like cadmium sulfide (CdS) and chromates like silver chromate (Ag_2CrO_4) can serve as photocatalysts, but their performance is hindered by the reduced photostability and hydrothermal stability. However, the activity can be improved by incorporating g-C_3N_4, and this material reduces charge obliteration and boosts the photocatalysis performance by increasing the photostability of such materials [173,174].

Moreover, the introduction of nanocomposites (rather than using pure components) can improve the properties and performance significantly. One such material is a silver niobate ($AgNbO_3$) composite with g-C_3N_4. This nanocomposite offers twofold higher performance compared with g-C_3N_4 due to the increased charge separation and higher absorbance range. Such materials offer a better solution for the photostability and performance of the material [164]. Certain precipitation and annealing approaches have been utilized to prepare ternary hybrid structures for photocatalytic water-splitting [175]. The surface area, morphology, and size of the material are the important factors determining the performance. One such example is the metal Co, which offers a large surface area-to-volume ratio (Table 2).

Modifications of the structure of the nanocomposite along with impurity atoms greatly impact the photodegradation efficiency in hierarchal modified TiO_2/g-C_3N_4 structures. Moreover, the porosity improved performance as compared to the neat g-C_3N_4. Fast charge dynamics, higher charge disjunctions, and increased absorbance greatly improved photocatalysis as depicted in Fig. 4 [176,177]. Fig. 4a schematically illustrates the g-C_3N_4 loaded TiO_2 NPs (TiO_2/g-C_3N_4) as proposed by Ranjithkumar et al., while band diagrams of TiO_2/g-C_3N_4 are shown in Fig. 4b. High-resolution transmission electron microscopy (HRTEM) confirmed the presence of pores in the image of nanocomposite and hence the successful synthesis of hierarchical *meso*/macro-porous structures as shown in Fig. 4c. Results of the specific capacitance of the prepared nanocomposites of TiO_2/g-C_3N_4 (denoted by TCN) are presented in Fig. 4d. 33 TCN showed the best results due to having the highest active surface area, which means greater diffusion of electrons at the surface of the electrode during redox reactions. Moreover, analysis of results from electrochemical impedance showed that 33 TCN exhibited the lowest internal electrolyte resistance, Fig. 4e, which coincides with its highest value of specific capacitance. The uniform and straight slope indicate the capacitive nature of the nanocomposite in the electrolyte. Hence, the most favorable capacitance was observed for an optimum loading of 33 % CN. The PL spectra displayed in Fig. 4f show suppression of nanofibers at 250–350 nm, which suggests lower photo-excited charge recombination efficiency of this nanocomposite. This may be due to the structure being beneficial for charge transfer and separation, which suppressed charge recombination. Photocurrents of TiO_2/g-C_3N_4 nanofibers under simulated solar light irradiation are shown in Fig. 4g. As is evident from the curve, the photocurrent density of the hierarchical *meso*/macro-porous structure of TiO_2/g-C_3N_4 was significantly higher than mesoporous TiO_2/g-C_3N_4 nanofibers. This result led us to conclude that the proposed hierarchical architecture of nanocomposite improved the light absorption ability and will lead to the production of photocurrents.

Certain materials show enhanced performance when coupled with other reagents like nickel ferrite ($NiFe_2O_4$) in the hydrogen generation

Table 2
Various heterojunctions and their corresponding fabrication techniques, related performances and intended application(s).

Heterojunction	Fabrication Technique	Substance Degraded	Performance	Intended Application(s)	Reference
g-C_3N_4–MnO_2 nanosheets	Wet chemical	Phenol	73.6 % degradation in 3 h	1. Solar-to-fuel conversion 2. Photocatalytic water treatment	[188]
g-C_3N_4–TiO_2 nanosheets	Hydrothermal treatment	MO	98 % degradation in 15 min	Overcoming environmental and energy-related problems	[189]
g-C_3N_4–$BiVO_4$ nanosheets	Calcination, hydrothermal	RhB	100 % within 1 h	1. Water treatment 2. Improving organic pollutant degradation	[190]
g-C_3N_4–TiO_2	Calcination	Formaldehyde (HCHO)	94 % degradation	Against indoor air pollution	[191]
FeS_2/g-C_3N_4 nanosheets	*In situ* hot injection	Cr (IV)	92.6 % removal in 2 h	Steering charge separation and transport in nanocomposites	[192]
		MB	99.8 % degradation in 2 h		
$BiVO_4$/g-C_3N_4	Calcination	Toluene	CO_2 generation rate of 13.9 ppm h^{-1}	Photocatalytic oxidation of toluene	[186]
Sr/g-C_3N_4	Photocatalytic method	NO_2	Decrease in conversion of secondary pollution rate from 62.5 % to 15.8 % for NO_2	Deep oxidation of NO	[193]
g-C_3N_4/AgCl/CDs	Impregnation	MB	98 % degradation in 126.25 h	Degradation of organic dyes	[194]
		RhB	90 % degradation in 126.25 h		
g-C_3N_4/MoS_2	p-SILAR	RhB	62 % degradation in 2 h	Detoxification of aqueous dye solutions	[195]
g-C_3N_4/ZnS/In_2S_3	p-SILAR	RhB	93.98 % dye degradation	For improvement in photochemical performance	[196]
g-C_3N_4/ZnO	Atomic layer deposition	MB	96.4 % dye degradation in 2 h	Enhancing photocorrosion resistance	[197]

reaction when introduced with zirconium dioxide (ZrO_2) [178]. The material showed a high performance after being calcinated at 700 °C (Table 3).

Specially designed nickel–iron oxide (Fe_2NiO) showed better performance in water-splitting when compared with the commercial Degussa due to its higher surface area to volume ratio and the better absorbance of the provided sunlight [179].

Certain noble metals and their hydroxides can be used for co-catalysis purposes. But the hydroxides are more economical, like nickel hydroxide $Ni(OH)_2$. A facile strategy can be employed to prepare the composites, and the hydrogen generation reaction efficiency improved for a composite of g-C_3N_4 with platinum, which is expensive. Another nanocomposite offers better performance as compared to conventional platinum and g-C_3N_4 nanocomposites. Noble metal oxides like silver oxide Ag_2O can be made into composites to tailor the performance of the g-C_3N_4 for H_2 generation reaction. Other nanocomposites offer better performance as compared to the conventional Pt and g-C_3N_4 nanocomposite. Noble metal oxides like Ag_2O can be used in composites to tailor the performance of the g-C_3N_4 for the H_2 generation reaction [169,180,181]. Wu et al. explained the mechanism of photocatalytic action of Ag_2O/g-C_3N_4 [182]. As schematically illustrated in Fig. 5a, the bottom of the CB for g-C_3N_4 is more negative (-1.12 eV) than that of Ag_2O (0.20 eV). In contrast, the top of the VB is more positive for g-C_3N_4 (1.7 eV) than that for Ag_2O (1.40 eV) [183–185]. This implies that photogenerated holes of g-C_3N_4 can be transferred to the higher VB of Ag_2O under irradiation of visible light. This is because of the higher redox potential of H^+/H_2 than CB of Ag_2O. Consumption of a greater number of holes means more photogenerated electrons can be used in photocatalytic H_2 evolution, which would increase the overall catalytic activity. The stability of these synthesized catalysts was tested under visible light irradiation after four intervals, each of 4 h. It can be seen in Fig. 5b that in the last run, about 92.86 μmol H_2 is generated within 4 h. H_2 evolution for different samples of Ag_2O/g-C_3N_4 is much higher compared to pure g-C_3N_4, as shown in the bar chart in Fig. 5c. Moreover, PL spectra show that the emission peak of Ag_2O/g-C_3N_4 is much lower in comparison to pure g-C_3N_4 as shown **in** Fig. 5d. It can be concluded that photocatalytic activity is enhanced by the addition of Ag_2O due to reduced electron-hole (e^-h^+) recombination. The enhanced activity is thus attributed to the tunability of the band gap, leading to higher charge segregation and thus high photocatalytic hydrogen generation [186]. To improve the performance, certain agents like boric acid can be utilized that provides a charge obliteration decrease and favorable mesoporosity in the structure. Such a case is observed when a boric acid solution is introduced into the Pt and g-C_3N_4 composite [187].

When exposed to sunlight, vacancy-introduced hybrid structures exhibited water degradation and hydrogen generation. Nitrogen-vacancy introduction of the g-C_3N_4 improved the charge disjunction. Thus, photocatalytic performance was high in contrast to the bulk structure. Photocurrent and electrochemical impedance spectroscopic analyses reinforced that vacancy modifications lead to unique morphologies that provide efficient absorbance of solar light, better activity, and increased generation of hydrogen fuel [177].

Certain bimetallic compounds can be added to g-C_3N_4 to achieve better water degradation performance. The use of the materials like nickel (Ni) and iron phosphides as bimetallic compounds in the g-C_3N_4 nanocomposites can improve H_2 generation as well as the degradation of organic compounds. A small percentage (around 5 %) of bimetallic phosphides experience maximal activity [198]. The ease of the protonation and reduced charge annihilation offer better results for the use of the ruthenium (Ru) and chlorine (Cl) with g-C_3N_4. Moreover, the charge carrier dynamics are also critical [199]. A novel nanocomposite that showed incredible performance and photostability has been designed containing copper (1) phosphide with g-C_3N_4 [200]. Correspondingly, the same material with a p-n heterojunction has been designed for improved photocatalytic hydrogen generation reaction and higher charge separation [201]. A novel composite containing Pt and ZrO_2 with

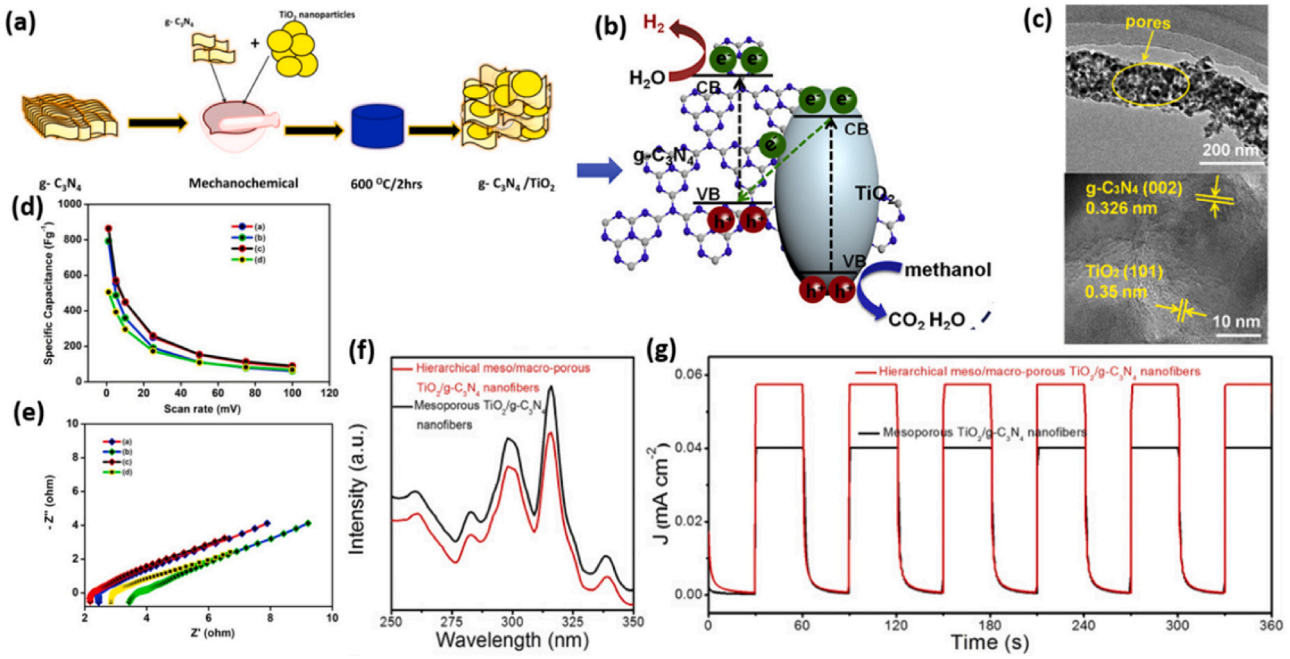

Fig. 4. (a) Schematic representation of synthesis of TiO_2/g-C_3N_4. (Reprinted with permission from Ref. [176] Copyright 2021 Elsevier). (b) Schematics of the band diagram of the nanocomposite. (c) TEM image of TiO_2/g-C_3N_4 showing mesoporosity and macroporosity as well. (Reprinted with permission from Ref. [177] Copyright 2021 Elsevier). (d) Improved cyclic voltammetry results attributed to enhanced surface area of absorption. (e) EIS displays increased specific capacitance due to faster charge carrier dynamics towards the surface of the charge collector in the nanocomposite. (Reprinted with permission from Ref. [176] Copyright 2021 Elsevier). (f) PL spectra show improved optoelectronic behavior. (g) Photocurrent strength exhibited improved absorbance and optoelectronics in the hierarchical and mesoporous nanocomposite as compared to the bulk. (Reprinted with permission from Ref. [177] Copyright 2021 Elsevier).

g-C_3N_4 has been synthesized that illustrates the impact of the band gap, work function, and charge separation on visible light-dependent water-splitting reactions [202].

Some other oxides like tungsten trioxide (WO_3) [203] and sulfides like nickel sulfide NiS [204] and molybdenum disulfide (MoS_2) [205] can be used as co-catalysts for better photocatalytic reactions of g-C_3N_4. Certain sulfides and titanates composited with g-C_3N_4 offer better performance as compared to neat g-C_3N_4 [206]. Fig. 6 illustrates the nanocomposites of g-C_3N_4 with strontium titanate ($SrTiO_3$), and the schematic illustration of photogenerated charges with the heterojunction and charge disjunction lead to better efficiency and high performance for water splitting as represented by the photoluminescence spectrum (PL). Efficient charge segregation offers an increase in absorbance and better photocatalytic performance [193,206,207]. Fig. 6a depicts the mechanism for the formation of NS/CN/STO composite as reported by Luo et al. [206]. This process could involve the initial adsorption of nanoplates of g-C_3N_4, followed by a reassembly process. $SrTiO_3$ NPs were used as a template for the self-assembly of g-C_3N_4 NPs and NiS. The synthesis process involves the following steps: (i) adsorption followed by wrapping of g-C_3N_4 NPs around the surface of $SrTiO_3$ NPs to minimize the net interfacial energy, (ii) reassembly of these adsorbed g-C_3N_4 NPs into a homogeneous layer, (iii) a subsequent application of an ion-exchange method for ensuring *in-situ* nucleation and growth of NiS on the surface of CN/STO, (iv) introduction of nickel acetate resulting in adsorption of Ni^{2+} ions on the surface of CN/STO, (v) and the addition of a Na_2S solution-induced hydrothermal reaction producing fine heterostructures of nanocomposites of NS/CN/STO. Luo et al. also proposed a possible mechanism for photocatalysis of a $SrTiO_3$ and g-C_3N_4 nanocomposite as schematically shown in Fig. 6b. Under the illumination of UV light, VB electrons of $SrTiO_3$ are excited to the CB, leaving behind holes in the VB. Under the illumination of visible light, electrons of g-C_3N_4 are excited from VB to VB, which leaves behind holes in its VB. Since the VB of $SrTiO_3$ is more positive than VB of g-C_3N_4, and the CB of g-C_3N_4 is more negative than the CB of $SrTiO_3$, the electrons from CB of g-C_3N_4 can be readily injected in $SrTiO_3$. This will provide easier transfer and separation of charges at the interface of both semiconductors, which implies less recombination of charge carriers. The CB levels of both g-C_3N_4 and $SrTiO_3$ are more negative than H_2 evolution levels, so they have good potential for H_2 production in water splitting. NiS is reported to have been a good cocatalyst for the production of H_2 via water splitting [208]. Therefore, it is used along with Pt NPs, which (together with NiS) increases the formation of active sites for H_2 evolution and enhances electron transfer in the NS/CN/STO photocatalyst. The even distribution of NiS NPs on the surface of 20 CN/STO was confirmed by TEM images shown in Fig. 6c. XRD patterns for the prepared 2NS/20CN/STO nanocomposite are shown in Fig. 6d. The peak corresponding to NiS is not visible, probably due to its low concentration and high dispersion in the prepared nanocomposite. An initial decrease followed by an increase in the intensity of PL emission can be seen in the PL spectra as shown in Fig. 6e. The broad and strong emission peak of g-C_3N_4 is an indication of rapid recombination of charged carriers. 20CN/STO showed a much lower PL emission peak, which is due to the formation of heterojunctions that lowered the rate of recombination and facilitated the separation of charges. The lowest PL emission intensity of 2NS/20CN/STO indicates suppression of rapid recombination due to the synergistic effects of heterojunction, the presence of NiS as a co-catalyst and closer contact between g-C_3N_4, NiS and $SrTiO_3$. Due to the remarkable role of NiS in enhancing charge separation, there is a significant increase in the photocatalytic activity of H_2 evolution. Transient photocurrent responses were measured to further investigate the mechanism of this improved photocatalytic activity. As shown in Fig. 6f, 2NS/20CN/STO resulted in the highest photocurrent density among all samples. This result proves the efficiency of NiS co-catalyst in electron transfer. Thus, 2NS/20CN/STO achieved the highest separation efficiency and best photocatalytic activity of H_2 evolution.

Table 3
Various g-C_3N_4 based photocatalysts and their degradation efficacy against harmful substances.

Photocatalyst	Precursor used	Key benefits	Pollutant degraded	Reference
Ag-doped g-C_3N_4	Melamine	Conductivity increased Lowering of energy barriers for reactions at interface	MB	[253]
MoS_2/g-C_3N_4	Dicyandiamide	Increase in absorption of visible light Efficient charge separation Greater surface area and active sites for reaction	MO	[254]
$ZnFe_2O_4$/g-C_3N_4	Melamine	Increased separation of electron-hole pairs Quicker separation from aqueous solution by magnet Increase in photocatalytic efficiency	MO	[255]
Fe(II)/ Graphene/g-C_3N_4	Urea	Increased absorption of visible light Reduced recombination of electron-hole pairs	MO	[256]
Pd-doped g-C_3N_4	Cyanamide	Electron trapping and hence increased separation of electron-hole pairs Increased absorption of visible light	Bis-phenol A	[257]
g-C_3N_4/g-C_3N_4	Thiourea and urea	Increased lifetime of charged carriers Effective separation of electron-hole pairs	RhB	[258]

Photodegradation of organic dyes

Mostly organic dyes are commonly used in the synthesis and preparation of edibles, ointments, clothing, leather goods, etc. However, these colored pigments are usually non-degradable and play a primary part in global water pollution. More than 10,000 variants of pigmented dyes are used annually in the fabric industry [209]. A major portion of such dyes is from azo-based compounds [150,151,210,211].

Dye contamination in drinking water causes serious health problems [212]. Some other materials like lipophiles actively contribute to water contamination due to their non-biodegradable nature. These materials must be destroyed or converted to non-hazardous materials before disposing of them in water. Aquatic and coastal regions are seriously damaged due to such pollutants even at very low contamination levels, resulting in severe damage. A promising method to address this issue is the use of solar light-driven nanomaterial-based semiconductor technology that degrades such materials into many useful and less harmful products. Various methods have been studied to degrade such harmful dyes. Certain nanocomposites have also been tailored and reported in this regard [213]. Sunlight-driven photocatalysis has the advantage of relying upon a renewable energy source [214,215].

Various studies have reported contaminated water treatment based on the photocatalysis process [216]. Such research provided a basic strategy for solar light-driven photocatalytic organic dye degradation. The primary step is that the material absorbs the incident light upon exposure to sunlight. The incident energy must be higher than the energy gap for photoexcitation of the respective material, otherwise, the incident light will not be absorbed. The next step involves the generation of charges, i.e., electrons and holes. After absorbing energy, the electron would move from a lower energy band towards a higher one, generating a hole in the valence band. Charge separation is necessary to improve the efficiency of the material. These photogenerated charges can migrate to the surfaces of the photocatalyst and induce chemical reactions. These reactions yield very reactive species like the superoxide and hydroxyl radicals that degrade the dyes into final less harmful products [217]. Certain dyes like methyl orange (MO), Rhodamine B (RhB), and methylene blue (MB) have been degraded by solar light-driven catalysis [216,218].

One such example is the use of a nanocomposite consisting of noble metal silver along with its salt silver bromide (AgBr) incorporated with g-C_3N_4 for degrading methyl orange by photocatalysis. The performance increased compared to the pure g-C_3N_4 due to the formation of the heterojunction of Ag nanoparticles [219]. Another composite for deteriorating RhB involves facet coupling between the bismuth bromide oxide (BiOBr) and the g-C_3N_4. The nanocomposite showed better performance due to the higher charge disjunction, resulting in higher photocatalysis and increased degradation of the organic dye [220]. Another material, bismuth iodide oxide (BiOI), was assembled using a heterojunction approach among g-C_3N_4 and porous materials. Respective heterojunctions displayed high performance due to the increased optical density of the solar light and increased charge disengagement [221]. A material with bismuth chloride oxide (BiOCl) and g-C_3N_4 was investigated for deteriorating a dye named MO, and the resulting heterojunctions provided the highest photocatalytic activity due to improved charge partition [222]. A nanocomposite consisting of the C_3N_4 along with Bi_2WO_6 resulted in higher efficiency of MD dye destruction due to effective charge disjunction [223]. Additionally, composites of certain phosphates with g-C_3N_4 (such as Ag_3PO_4) were prepared using the precipitation route. The nanocomposite displays higher performance than g-C_3N_4 due to the synergistic effects of the nanocomposite and a morphology that provides a higher surface area-to-volume ratio [155].

Oxide nanocomposites with g-C_3N_4 show better photocatalytic degradation due to the higher charge separation and boosted charge carrier dynamics. One such example is the use of the cerium oxide (CeO_2) and g-C_3N_4 heterojunction, which strengthens the sunlight-dependent destruction of MB [224]. Another example of such oxide-strengthened g-C_3N_4 is the use of TiO_2. Fig. 7 illustrates the deposition of TiO_2 on g-C_3N_4 and the respective results for photocatalytic destruction of RhB dye. The respective rate of the reaction for the material synthesized by ALD was 3 times higher than neat g-C_3N_4 due to enhanced charge disjunction [38]. Fig. 7a shows the degradation kinetics of Rh dye in different compounds under the irradiation of visible light with respect to time. Although all tested samples showed photocatalytic activities, it is interesting to note that even though pure TiO_2 is incapable of absorbing visible light due to its large band gap, it still removed around 32 % of RhB dye molecules due to the phenomenon of dye sensitization which occurs on the surface of TiO_2 due to RhB adsorbed on it. This result was also confirmed by previous studies as also reported by Wu et al. [225]. Fig. 7b shows the rate constants for the reaction of the samples. As is evident from the chart, TiO_2 showed the lowest rate reaction constant followed by g-C_3N_4. It is also apparent that when ALD cycles increased from 2 to 5 (GT2 to GT5 in the chart), there was a significant increase in rate constants. However, a subsequent increase in ALD cycles led to a decrease in the value of rate constants.

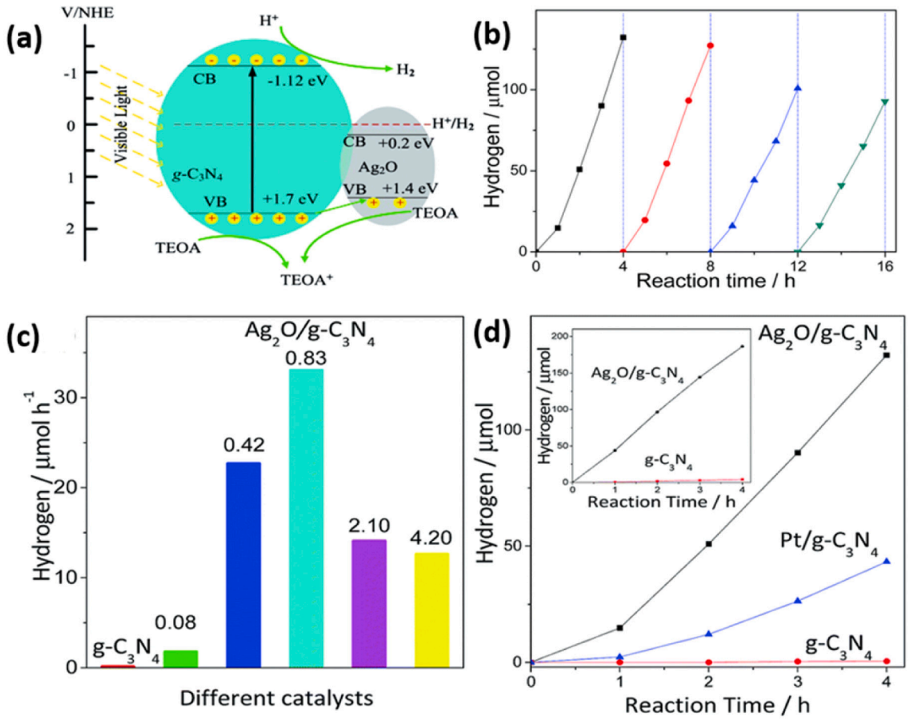

Fig. 5. (a) Schematic illustration of photocatalysis $Ag_2O/g\text{-}C_3N_4$ exposed to sunlight. (b) Stability of the HER. (c), (d) Rate of HER for various weight ratios of the nanocomposite exposed to visible light, exhibiting the maximum rate at Ag_2O:$g\text{-}C_3N_4$ = 0.83. (Reprinted with permission from Ref. [182] Copyright 2015 RSC).

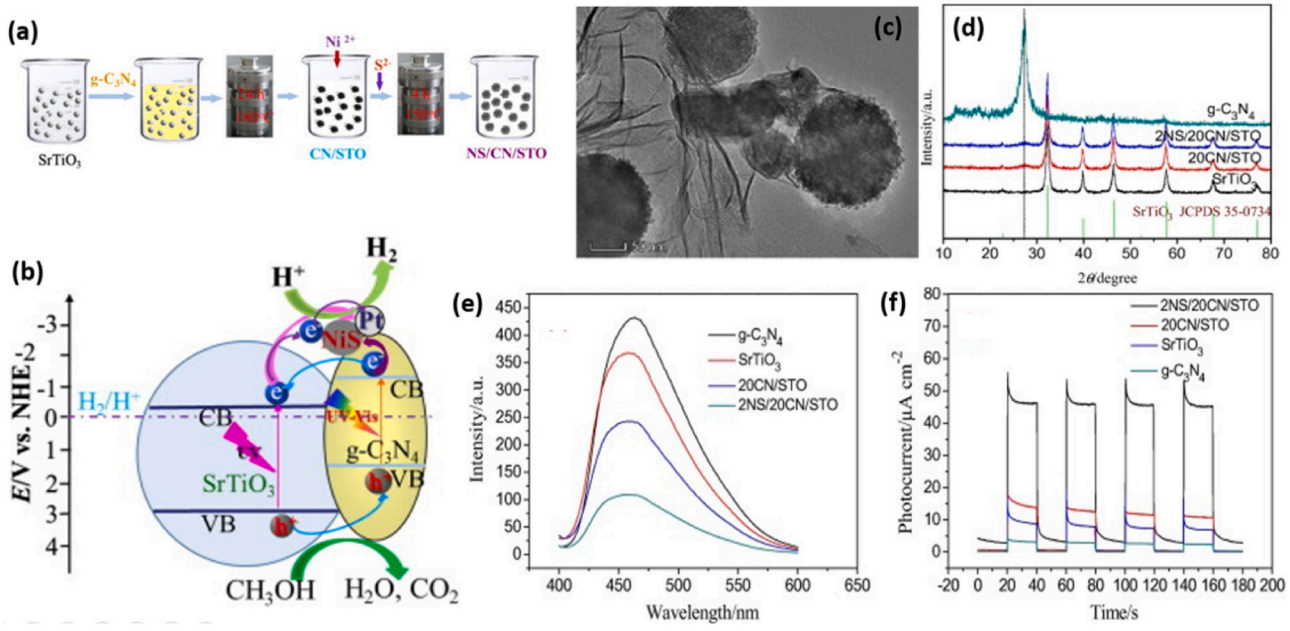

Fig. 6. (a) Schematic synthesis of $NiS/g\text{-}C_3N_4/SrTiO_3$ composites. (b) Schematic illustration of photocatalysis of $SrTiO_3$ and $g\text{-}C_3N_4$ nanocomposite. (c)TEM image of composite. (d) X-ray diffraction analysis patterns of various materials show better absorption, better surface area, and reduced charge disjunction. (e) Photoluminescence spectra of various materials and (f) transient photocurrent responses (reprinted with permission from Ref. [206] Copyright 2018 Elsevier).

Therefore, it is essential to control the amount of $g\text{-}C_3N_4$ in GTs for efficient photocatalysis. Fig. 7c presents the percentage by weight of $g\text{-}C_3N_4$ in GTs with respect to ALD cycles. As shown in the graph, an abrupt decrease in concentration of $g\text{-}C_3N_4$ was recorded when ALD cycles were increased from 2 to 200. Therefore, it was necessary to normalize the rate constant to the concentration of $g\text{-}C_3N_4$ in GTs as shown in Fig. 7d. It is easy to observe from the graph that only 5 ALD cycles are required to reach the saturated photocatalytic reaction rate constant. To further understand this behavior, the charge recombination behavior and specific surface area of GTs were determined as they dictate the photocatalytic reaction rate constant. As shown in Fig. 7e, which shows PL emission, $g\text{-}C_3N_4$ showed the highest intensity, which indicates its largest rate of charge recombination and lowest photoactivity. PL intensity significantly decreased as the number of ALD cycles increased

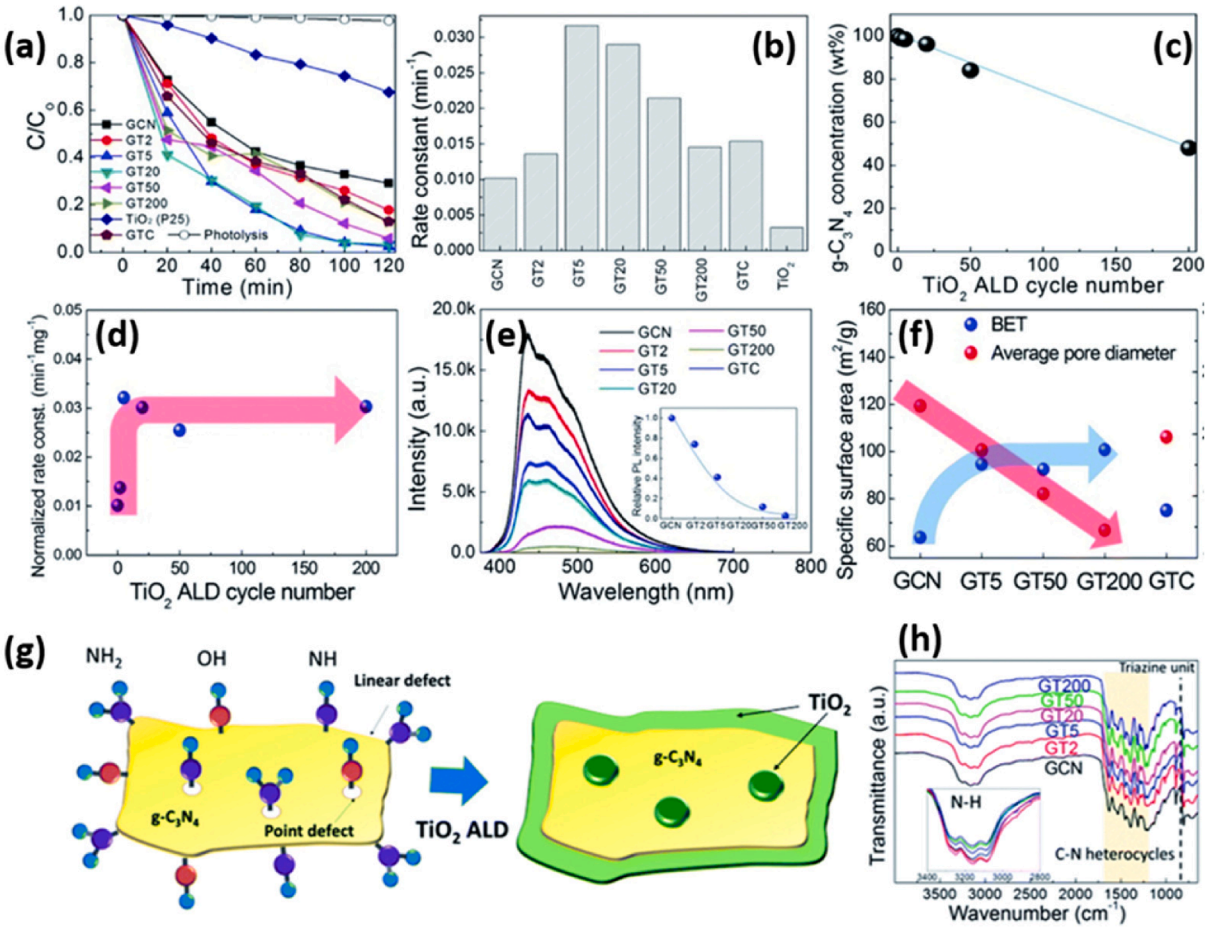

Fig. 7. (a) Degradation of RhB dye under influence from various compounds of g-C_3N_4 and pure TiO_2. (b) Comparison of rate constants of compounds. (c) Percentage by weight of g-C_3N_4 in GTs. (d) Plot of normalized rate constant against cycles of ALD. (e) Results from PL emission spectroscopy. (f) BET analysis of compounds. (g) Growth mechanism of TiO_2 on g-C_3N_4. (h) Results from FTIR spectroscopy. (Reprinted with permission from Ref. [38] Copyright 2019 RSC).

from 2 to 5 and then saturated gradually over 5 cycles of ALD. Thus, 5 cycles of ALD were optimum for effective separation of charges. Similarly, the results of BET presented in Fig. 7f show that the specific surface area initially increased, but it saturated after 5 ALD cycles due to decrease in average pore size with increasing TiO_2 ALD cycles. Fig. 7g provides a clue to the reason for this interesting result. It shows that TiO_2 nucleates at the defected sites on the surface and edges of g-C_3N_4 have NH, NH_2, and OH functional groups. FTIR spectra shown in Fig. 7h further confirm that the increase in the number of ALD cycles can change the defect sites and decrease the surface-active species as they are consumed by ALD TiO_2 growth.

Another oxide molybdenum trioxide (MoO_3) has been designed with g-C_3N_4 to achieve better results after exposure to the visible radiations of solar light. Here, the increased efficiency is related to the efficient charge dynamics and decreased recombination [226]. Fig. 8 provides a schematic illustration of the novel material containing MoO_3 with g-C_3N_4. Enhanced photodeterioration of the organic dye was achieved due to the increased charge separation and reduced recombination [114,115]. Huang et al. proposed the synthesis of MoO_{3-x}/g-C_3N_4 nanocomposite by a mild solvothermal method, which employed C_2H_5OH as a reductive agent for the introduction of oxygen vacancy to narrow the band gap, enhancing the light absorption range and decreasing the recombination of photoexcited charge carriers, while its 1D structure will prolong the lifetime of charged carriers [227]. Fig. 8a schematically illustrates the reaction for the formation of yellow power (g-C_3N_4) and Fig. 8b depicts the reaction sequence to obtain the MoO_{3-x}/g-C_3N_4. A schematic diagram showing the mechanism of transport and separation of e^--h^+ pairs at the interface of MoO_3/g-C_3N_4 is presented in Fig. 8c. As the CB potential of MoO_3 is less negative than that of g-C_3N_4, transfer of electrons takes place from g-C_3N_4 to MoO_3 while the movement of holes is from MoO_3 to g-C_3N_4 due to the great difference in their respective VB potentials. Therefore, the net photocatalytic activity is enhanced due to the effective separation of charges and reduced recombination effect. An SEM image of g-C_3N_4/MoO_3 (7 % composite) shows that an amorphous layer of CN polymers is wrapped around the crystalline MoO_3 particles (Fig. 8d). Further accurate morphological analysis by HRTEM showed that the outermost boundary of these MoO_3 particles is the g-C_3N_4 layer (Fig. 8e). A heterojunction structure formed and improved the net photocatalytic activity of this nanocomposite as discussed previously. Fig. 8f confirms that obtained values of E_g of g-C_3N_4 and MoO_3 are 2.70 eV and 2.92 eV, respectively. This result agrees with previously reported literature [228,229]. Fig. 8g shows the photocatalytic degradation efficiencies of different concentrations of g-C_3N_4. It is evident from these curves that photocatalytic efficiency is governed by the amount of g-C_3N_4. The result indicates that the optimum concentration of g-C_3N_4 is 7 %. Another factor that is crucial for good photocatalytic efficiency is the stable nature of the photocatalyst. The stability of g-C_3N_4/MoO_3 was confirmed as it did not exhibit a significant loss after 5 cycling runs for MB photodegradation under visible light irradiation.

Different morphological structures (like using porous Fe_3O_4 along with g-C_3N_4) have contributed to the photocatalytic behavior of the MO dye degradation [230]. Furthermore, a nanocomposite containing sodium tantalate ($NaTaO_3$) and g-C_3N_4 displayed better performance for

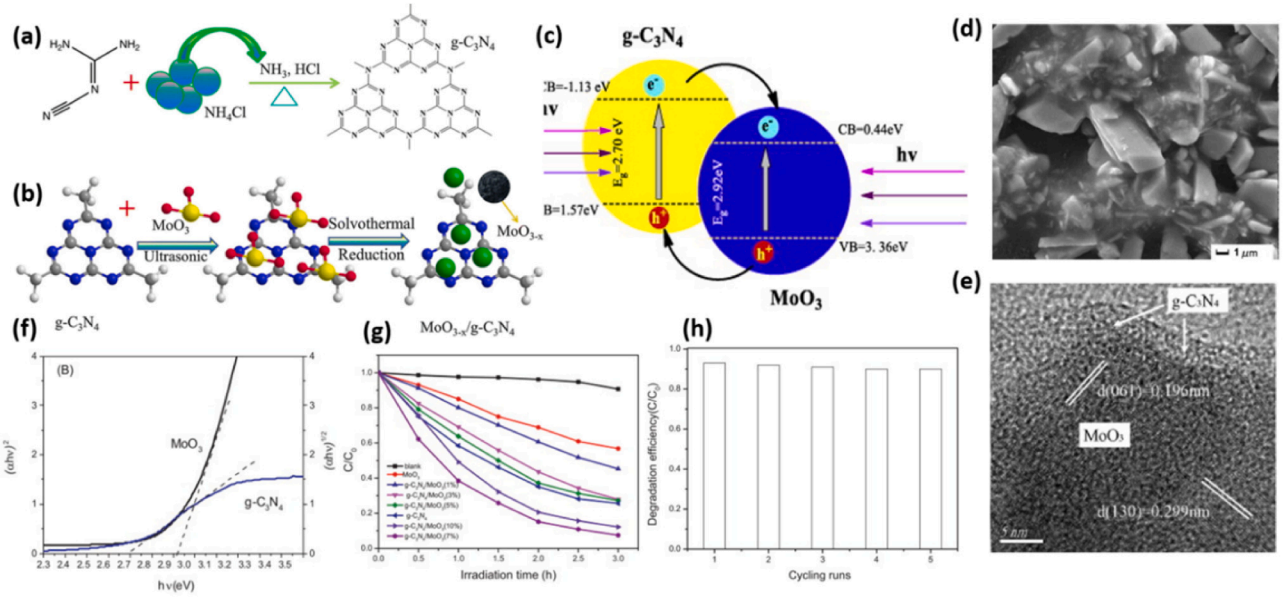

Fig. 8. Schematics of reactions involved in the synthesis of (a) g-C_3N_4 and (b) MoO_{3-x}/g-C_3N_4. (Reprinted with permission from Ref. [227] Copyright 2018 Springer). (c) A possible mechanism for photodegradation of MB on g-C_3N_4/MoO_3. (d) SEM image of g-C_3N_4/MoO_3 (7 %). (e) HRTEM image of g-C_3N_4/MoO_3 (7 %) composite. (f) Plot of $(ah)^2$ against energy in eV. (g) Comparison of efficiencies of various compounds in photocatalytic degradation. (h) A measure of photocatalytic degradation of g-C_3N_4/MoO_3 (7 %) through cycling runs. (Reprinted with permission from Ref. [226] Copyright 2013 Elsevier).

deterioration of the RhB dye. So, charge carrier dynamics and the charge partition are important steps for strengthening the process [231]. A hybrid material consisting of silver halide and g-C_3N_4 exhibits better performance [87]. Certain sulfides like MoS_2 incorporated along with g-C_3N_4 appeared beneficial for photo-driven deterioration of the MB [232]. Other strategies involve nanocomposites fabricated for the solar light-driven organic dye deterioration, structures like titania accompanied by silica nano-composited with g-C_3N_4 QDs [233], or even simply titania with g-C_3N_4 [234], molybdenum sulfide with g-C_3N_4 [205], or altered g-C_3N_4 [235]. In other applications titania accompanied g-C_3N_4 was used to treat RhB [236], g-C_3N_4 modified with $BiPO_4$ was used to destroy orange G [24], while g-C_3N_4 was fabricated with 1,3,5-benzenetriyl [237].

Another nanocomposite containing TiO_2 and g-C_3N_4 offers reduced charge recombination and higher segregation. The lanthanum ions trap charges and suppress the charge recombination, thus enhancing the dye degradation based on a synergistic response between TiO_2, g-C_3N_4, and the metallic ions. Fig. 9 depicts the unique morphological symmetry of such material along with the high charge separation efficiency and a strong interface, leading to dye deterioration [238]. Li et al. determined the mechanisms for the La_xTiCN heterojunction catalyst as shown in Fig. 9a. The first step is the infiltration of Ti precursor between the gaps of lamellae of g-C_3N_4 followed by growth of TiO_2 crystal and formation of a sheet-like structure. Lamellae of g-C_3N_4 were placed in descending

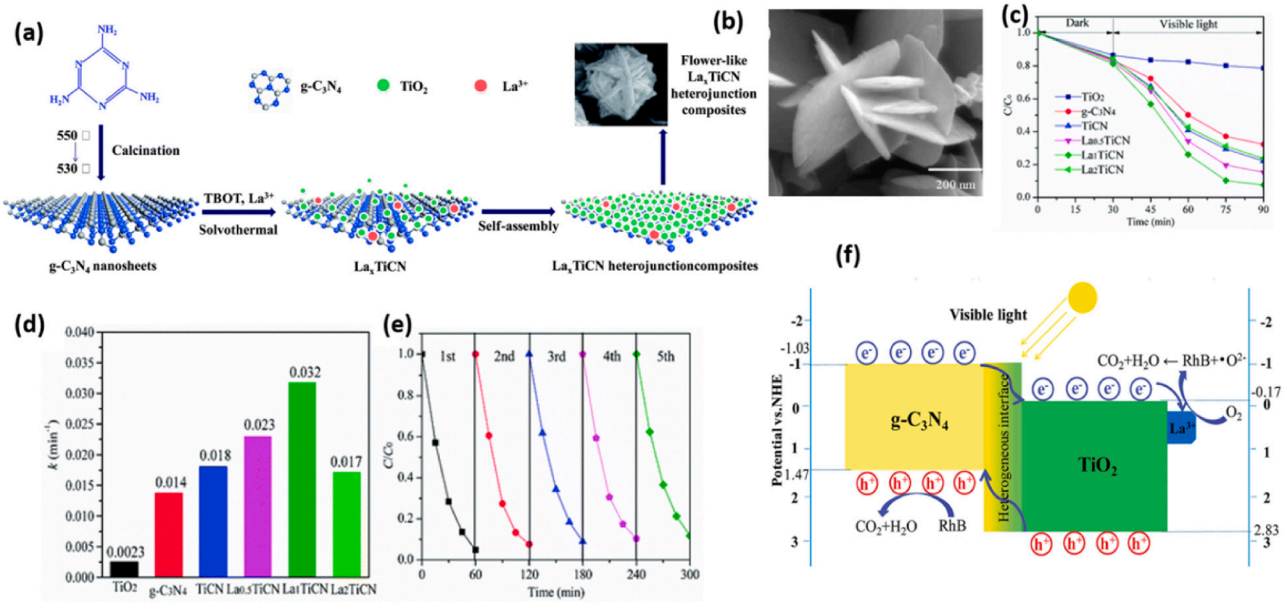

Fig. 9. (a) Mechanism of La_xTiCN formation. (b) SEM micrograph of g-C_3N_4-TiO_2. (c) RhB dye photocatalytic degradation versus time. (d) Results of calculated pseudo-first-order rate constant k_{app} for each sample. (d) Efficacy of La_1TiCN in the removal of RhB dye and comparison with various other compounds. (e) Schematic illustration of g-C_3N_4 -TiO_2 for RhB degradation. (f) Band gap diagram of the nanocomposite. (Reprinted with permission from Ref. [238] Copyright 2018 RSC).

order of size with La^{3+} deposited on the surface of the crystal. The obtained composite of La_xTiCN resembles a flower-like structure, and it was formed via self-assembly. Fig. 9b shows the SEM image of flower-shaped 3D TiO_2 formed after alternatively arranged lamellae approximately 500 nm in length. Photocatalytic efficiencies of various samples were determined under visible light irradiation degradation of RhB dye as shown in Fig. 9c. As is apparent in the graph, La_1TiCN exhibited the best overall photocatalytic activity. The dense hetero interface formed between TiO_2 and g-C_3N_4 could be the reason for effective electron-hole transfer. La_1TiCN also resulted in the highest value of first-order rate constant (k_{app}) as shown in the chart in Fig. 9d. Moreover, La_1TiCN showed a reduction of 95.2 % to 88.3 % in the photocatalytic efficiency of RhB after 5 cycles. This result confirmed the lower photo-corrosion and good stability of La_1TiCN, making it a novel method for treatment of wastewater. The proposed heterojunction degradation mechanism of La_xTiCN is schematically illustrated in Fig. 9e. The closer interface between TiO_2 and g-C_3N_4 facilitates the passage of electrons, which ultimately increased the net transfer of photoelectrons. With the introduction of an appropriate amount of La, the interface barrier became larger, and the space charge region became narrower. Recombination of e^--h^+ is considerably suppressed due to the large electric field and the orientation of electrons of g-C_3N_4 between TiO_2 and La. The incorporation of La^{3+} can increase the efficiency of e^--h^+ separation, which enhanced the net photocatalytic efficiency.

Photodegradation of harmful volatiles

In addition to the destruction of organic dyes for the treatment of wastewater disposal, certain other issues like removal of the non-ecofriendly gases from the atmosphere can be addressed using light-dependent reactions. One such example is the aromatic gases produced by the combustion of methane gas [239]. An aromatic gas called toluene can be degraded successfully by the solar light-driven degradation process by incorporating $BiVO_4$ and g-C_3N_4 [186]. The enhanced activity of the material was attributed to the nanocomposite heterojunction, high surface area to volume ratio, increased optical density, and the high disjunction of electrons and holes.

Certain noble metals in small concentrations can be effective. For example, Ag along with g-C_3N_4 can improve the properties due to reduced electron-hole recombination and increases in the photocatalytic deterioration of the aromatic gas [240]. Notably, Mn significantly affects the process of the degradation of the harmful volatile components when being used as a nanocomposite with g-C_3N_4 [241]. Anatase-modified g-C_3N_4 structures play a vital role in the solar light-driven deterioration of harmful gases like methyl benzene due to the synergies of using both materials [242]. Certain hybrids consisting of metal (like Ag) along with its phosphate (Ag_3PO_4) combined with g-C_3N_4 can degrade carbolic acid in the solar light-driven deterioration process [243]. The impact of titania added to g-C_3N_4 also helps to degrade the carbolic acid when exposed to solar light [180]. Moreover, certain other materials like graphene can be added to g-C_3N_4 to degrade the phenylic acid photochemically [181]. Certain oxides like Ag_2O cooperate with g-C_3N_4 to improve the destruction of carbolic acid (C_6H_6O) [244]. Ternary hybrid structures like Co-doped g-C_3N_4 supported with anatase can serve to efficiently degrade phenylic acid [245]. NO is an elemental source of environmental pollution, making it difficult to fully degrade. This can be achieved through solar light-dependent photocatalysis. Certain noble metals like palladium (Pd) composites with g-C_3N_4 can destroy such volatile gaseous contaminants. The destruction process follows a similar mechanism and results in less hazardous products [246].

Another strategy involves the use of bismuth subcarbonate ($(BiO)_2CO_3$) with g-C_3N_4 for photo-dependent deterioration of NO [247]. Introducing certain vacancies and defects in the material g-C_3N_4 can also increase nitrogen defects, resulting in one of the highest photocatalytic responses compared to the noble material. This performance was attributed to the reduction in the band gap, pronounced charge disjunction, and the impact of the defects in the material [248,249]. Certain doping strategies can improve the charge disjunction and the absorption of sunlight, resulting in better performance as in bismuth molybdenum oxide (Bi_2MoO_6). The generation of active species during photocatalysis (like hydroxyl radicals) can improve the deterioration of NO or even further degrade it to less harmful entities [248].

Certain noble metals also accelerate the process of photodegradation in contrast to neat g-C_3N_4, like Au added to g-C_3N_4 to deteriorate nitric oxide due to the reduced recombination, morphology, and charge carrier dynamics [250]. Ions like K^+, Ca^{2+}, and PO_4^{3-} can also work well with the g-C_3N_4 to degrade the NO [251,252]. Moreover, the introduction of K^+ and chloride Cl^- ions resulted in high performance due to higher optical density and enhanced charge disjunction. O_2 and K

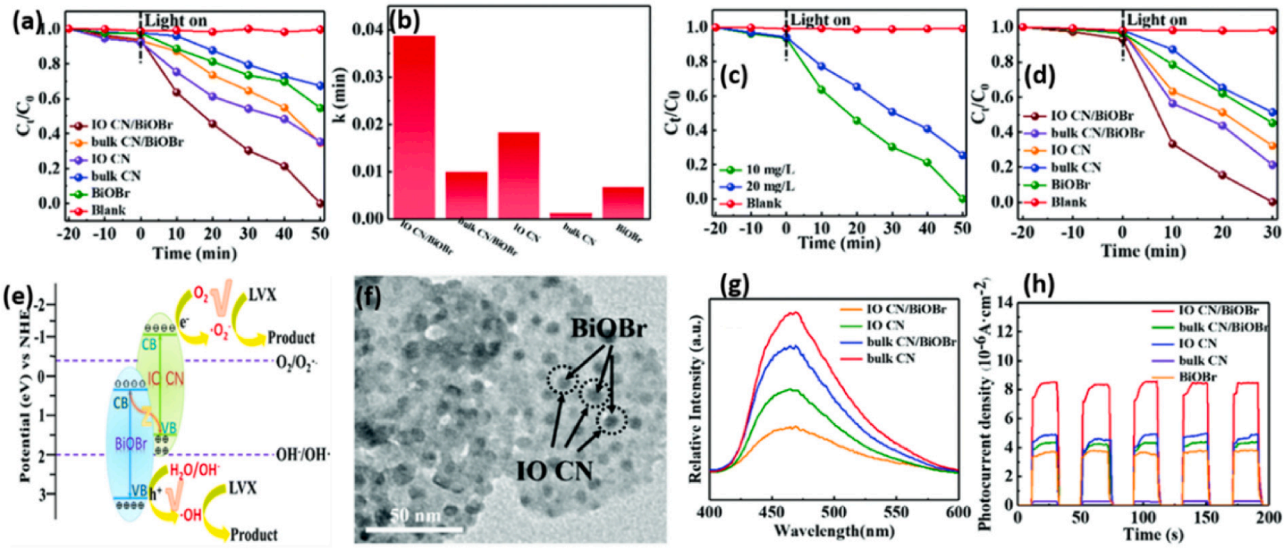

Fig. 10. (a) Photocatalytic degradation rates of LVX over different catalysts and (b) the corresponding rate constant. (c) Comparison of degradation results for LVX at different concentrations, and (d) the degradation results for RhB over different catalysts under visible light irradiation. (e) Proposed scheme of charge transfer in IO CN/BiOBr. (f) HRTEM micrograph of IO CN/BiOBr. (g) Results of PL spectra of various photocatalysts. (h) Transient photocurrent responses of different photocatalysts. (Reprinted with permission from Ref. [260] Copyright 2019 RSC).

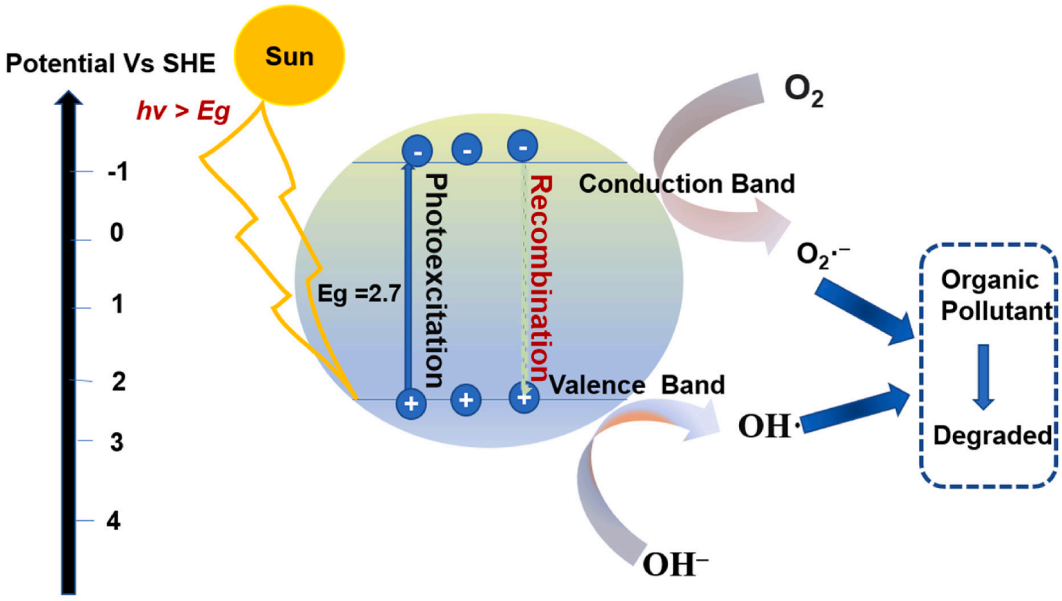

Scheme 4. A schematic illustration depicting mechanism of photocatalysis for g-C_3N_4.

incorporated g-C_3N_4 can also promote photo-dependent deterioration of the NO due to the enhanced reactive species [193,207].

Medical industry wastewater sources are toxic to waterborne life, causing a global pollution problem. The management and disposal of such materials are thus necessary. Renewable energy-dependent reactions like photocatalysis can address this problem [207,259]. In this regard, several studies have been reported like nanocomposites of g-C_3N_4 with BiOBr accompanied by silica material resulting in efficient degradation [260]. Bin Chen et al. evaluated the photocatalytic activity of catalysts by monitoring the photocatalytic degradation of antibiotics. The antibiotics are represented by LVX in Fig. 10. As shown in Fig. 10a, the rate of degradation recorded over bulk CN/BiOBr was 34.5 % after 50 min of continuous visible light irradiation. In contrast, it was merely 54.6 % over pure BiOBr and 23.6 % over IO CN. However, LVX was shown to fully degrade within 50 min over IO CN/BiOBr. It can be concluded from these results that IO CN/BiOBr has greater photocatalytic action than its bulk counterparts. Fig. 10b shows a comparison of photocatalytic performance using photocatalytic degradation rate constants. As shown, the rate constant of IO CN/BiOBr is 5.5x greater than that of bulk CN/BiOBr, suggesting that the activity of the photocatalyst can be increased by inverse opal construction. Moreover, the mean value of the rate constant for IO CN/BiOBr is 2.3x more than that of IO CN due to the introduction of BiOBr catalyst. When coupled, IO CN and BiOBr showed a significant increase in the overall photocatalytic activity of both parts. Fig. 10c further confirms the outstanding photocatalytic action of IO CN/BiOBr as the rate of degradation for LVX antibiotic was 25.5 % in 50 min as the concentration increased to 20 mg/L. We note here that IO CN/BiOBr can also be used for the degradation of several other types of contaminants including azo dye RhB. Fig. 10d illustrates the degradation profile for RhB. As is evident from the graph, RhB was fully degraded within 30 min, with IO CN/BiOBr yet again exhibiting the greatest photocatalytic action. These results suggest that as-prepared IO CN/BiOBr can be used against a variety of organic pollutants in wastewater. A possible mechanism of photocatalytic action (Z-scheme) and transfer of charge in IO CN/BiOBr is schematically illustrated in Fig. 10e. HRTEM was employed to analyze the chemical composition of as-prepared IO CN/BiOBr. Fig. 10f shows the uniform introduction of BiOBr NPs on the surface of IO CN. The degree of recombination in photo-generated carriers was measured based on the photoluminescence (PL) intensity. As shown in Fig. 10g, the curves of intensity for various catalysts are in reasonable agreement with their respective photocatalytic performances as IO CN/BiOBr shows the lowest intensity in PL spectra. To further validate this, the photocurrent test (POL) was employed. It is evident from Fig. 10h that the photocurrent response of IO CN/BiOBr showed a remarkable increase in comparison to other photocatalysts, indicating a lower degree of recombination rate with more effective separation of photogenerated electron-hole pairs.

Certain nanosheets of g-C_3N_4 along with copper sulfides have been prepared for the destruction of waste levofloxacin exposed to sunlight 259.The performance of $Cu_{2-x}S$ composites with g-C_3N_4 exposed to visible light was elucidated in the near-infrared region of the solar spectrum. Increased efficiency of photocatalytic deterioration was observed. Additionally, some tri-junctions like rubidium chloride along with bismuth sub carbonate and g-C_3N_4 showed effective destruction of tetracycline hydrochloride [260]. Hydrogen peroxide (H_2O_2) is a primary material due to its many applications. It can be prepared using composites of g-C_3N_4 with NiCoP or CoP following a solar light-driven photochemical reaction [10,199].

Summary and future concerns

The combination of g-C_3N_4 with metals, non-metals, or semiconductors yields better results in the photocatalytic applications of water splitting, organic dye deterioration, and degradation of harmful volatile species. Nanocomposites of g-C_3N_4 greatly impact the photodegradation process, resulting in improved optical density and absorbance of the incident sunlight illustrated by Scheme 4.

Incorporating semiconductors strengthened the absorbance capacity by tuning the band gap alignment of the resulting material by increasing the absorbance range from the ultraviolet to the visible region of the solar spectrum. Moreover, the detrimental charge recombination could also be avoided. Greater charge disjunction results in greater material efficiency. Thus, the overall photocatalytic process involves **a)** absorbance of incident light, **b)** photogeneration of e-holes, **c)** charge carrier transport, **d)** redox reactions and the creation of active species, and **e)** charge recombination. Certain modifications like surface area increases, morphology modifications, the introduction of co-catalysts, defect control, control of back-oxidation reactions, and control of mass-transfer limitations and heterojunction can improve the photocatalysis reaction. So, strategies to synthesize and modify the photoactive properties of g-C_3N_4 can be summarized as follows.

- The limited optical tunability of g-C_3N_4 is restricted to the ultraviolet region of the solar spectrum i.e., around 5–7 %, while most of the sunlight is not absorbed. Thus, adjusting and expanding the surface area of the material to enhance the absorbance of the sunlight is required for photocatalytic applications.
- Despite having advantageous band gaps, charge carrier dynamics, and electronic behavior, there are certain reasons for the transfer of electronic charges. Moreover, the ability of the material to be incorporated into biological platforms as a multi-indicating and multi-monitoring system still requires assessment.
- The conversion efficiency of the material for redox reactions and generation of reactive radical species is yet to be assessed.
- The aggregation and toxicity of the material must still be thoroughly accessed.

Based on this review, we predict that pristine g-C_3N_4 and its nanocomposites will find use in advanced materials applications including but not limited to solar energy applications.

CRediT authorship contribution statement

Aleena Azhar: Writing – original draft. **Muhammad Aanish Ali:** Writing – review & editing. **Ijaz Ali:** Formal analysis. **Tae Joo Park:** Resources, Supervision. **Muhammad Abdul Basit:** Conceptualization, Supervision.

Declaration of Competing Interest

The authors declare that they have no known competing financial interests or personal relationships that could have appeared to influence the work reported in this paper.

Data availability

Data is already reflected in the paper through figures.

Acknowledgements

Research review work was mainly done at Department of Materials Science and Engineering at Institute of Space Technology, Pakistan while technical support was furnished by Nanodevice Engineering Laboratory, Hanyang University South Korea from Project No. 20010727 (Technology Innovation Program by Ministry of Trade, Industry and Energy Korea).

References

[1] X. Fang, Q. Shang, Y. Wang, L. Jiao, T. Yao, Y. Li, Q. Zhang, Y. Luo, H. Jiang, Single Pt atoms confined into a metal–organic framework for efficient photocatalysis, Adv. Mater. 30 (2018) 1705112.
[2] Y. Huang, Y. Liang, Y. Rao, D. Zhu, J. Cao, Z. Shen, W. Ho, S.C. Lee, Environment-friendly carbon quantum dots/$ZnFe_2O_4$ photocatalysts: characterization, biocompatibility, and mechanisms for NO removal, Environ. Sci. Technol. 51 (2017) 2924–2933.
[3] Q. Zheng, D.P. Durkin, J.E. Elenewski, Y. Sun, N.A. Banek, L. Hua, H. Chen, M. J. Wagner, W. Zhang, D. Shuai, Visible-light-responsive graphitic carbon nitride: rational design and photocatalytic applications for water treatment, Environ. Sci. Technol. 50 (2016) 12938–12948.
[4] M.R. Hoffmann, S.T. Martin, W. Choi, D.W. Bahnemann, Environmental applications of semiconductor photocatalysis, Chem. Rev. 95 (1995) 69–96.
[5] Z. Zou, J. Ye, K. Sayama, H. Arakawa, Direct splitting of water under visible light irradiation with an oxide semiconductor photocatalyst, Nature 414 (2001) 625–627.
[6] X. Gong, D. Huang, Y. Liu, Z. Peng, G. Zeng, P. Xu, M. Cheng, R. Wang, J. Wan, Remediation of contaminated soils by biotechnology with nanomaterials: bio-behavior, applications, and perspectives, Crit. Rev. Biotechnol. 38 (2018) 455–468.
[7] D. Huang, Y. Wang, C. Zhang, G. Zeng, C. Lai, J. Wan, L. Qin, Y. Zeng, Influence of morphological and chemical features of biochar on hydrogen peroxide activation: implications on sulfamethazine degradation, RSC Adv. 6 (2016) 73186–73196.
[8] D. Huang, X. Wang, C. Zhang, G. Zeng, Z. Peng, J. Zhou, M. Cheng, R. Wang, Z. Hu, X. Qin, Sorptive removal of ionizable antibiotic sulfamethazine from aqueous solution by graphene oxide-coated biochar nanocomposites: influencing factors and mechanism, Chemosphere 186 (2017) 414–421.
[9] D. Huang, X. Guo, Z. Peng, G. Zeng, P. Xu, X. Gong, R. Deng, W. Xue, R. Wang, H. Yi, White rot fungi and advanced combined biotechnology with nanomaterials: promising tools for endocrine-disrupting compounds biotransformation, Crit. Rev. Biotechnol. 38 (2018) 671–689.
[10] L. Bi, X. Gao, L. Zhang, D. Wang, X. Zou, T. Xie, Enhanced photocatalytic hydrogen evolution of NiCoP/g-C_3N_4 with improved separation efficiency and charge transfer efficiency, ChemSusChem 11 (2018) 276–284.
[11] S. Cao, J. Low, J. Yu, M. Jaroniec, Polymeric photocatalysts based on graphitic carbon nitride, Adv. Mater. 27 (2015) 2150–2176.
[12] J. Liu, Y. Liu, N. Liu, Y. Han, X. Zhang, H. Huang, Y. Lifshitz, S.-T. Lee, J. Zhong, Z. Kang, Metal-free efficient photocatalyst for stable visible water splitting via a two-electron pathway, Science 347 (2015) 970–974.
[13] M. Alhaji, K. Sanaullah, A. Khan, A. Hamza, A. Muhammad, M. Ishola, A. Rigit, S. Bhawani, Recent developments in immobilizing titanium dioxide on supports for degradation of organic pollutants in wastewater-A review, Int. J. Environ. Sci. Technol. 14 (2017) 2039–2052.
[14] X. Ma, W. Ma, D. Jiang, D. Li, S. Meng, M. Chen, Construction of novel WO_3/$SnNb_2O_6$ hybrid nanosheet heterojunctions as efficient Z-scheme photocatalysts for pollutant degradation, J. Colloid Interface Sci. 506 (2017) 93–101.
[15] Q. Sun, K. Lv, Z. Zhang, M. Li, B. Li, Effect of contact interface between TiO_2 and g-C_3N_4 on the photoreactivity of g-C_3N_4/TiO_2 photocatalyst:(0 0 1) vs (1 0 1) facets of TiO_2, Appl. Catal. B Environ. 164 (2015) 420–427.
[16] S. Yan, Z. Li, Z. Zou, Photodegradation of rhodamine B and methyl orange over boron-doped g-C_3N_4 under visible light irradiation, Langmuir 26 (2010) 3894–3901.
[17] C. Zhou, C. Lai, P. Xu, G. Zeng, D. Huang, C. Zhang, M. Cheng, L. Hu, J. Wan, Y. Liu, In situ grown AgI/$Bi_{12}O_{17}Cl_2$ heterojunction photocatalysts for visible light degradation of sulfamethazine: efficiency, pathway, and mechanism, ACS Sustain. Chem. Eng. 6 (2018) 4174–4184.
[18] Z. Sun, J.M.T.A. Fischer, Q. Li, J. Hu, Q. Tang, H. Wang, Z. Wu, M. Hankel, D. J. Searles, L. Wang, Enhanced CO_2 photocatalytic reduction on alkali-decorated graphitic carbon nitride, Appl. Catal. B Environ. 216 (2017) 146–155.
[19] Y. Zhang, L. Li, Q. Han, L. Tang, X. Chen, J. Hu, Z. Li, Y. Zhou, J. Liu, Z. Zou, Bi_2MoO_6 nanostrip networks for enhanced visible-light photocatalytic reduction of CO_2 to CH_4, ChemPhysChem 18 (2017) 3240–3244.
[20] J. Pan, Y. Sheng, J. Zhang, J. Wei, P. Huang, X. Zhang, B. Feng, Preparation of carbon quantum dots/TiO_2 nanotubes composites and their visible light catalytic applications, J. Mater. Chem. A. 2 (2014) 18082–18086.
[21] C. Zhou, C. Lai, C. Zhang, G. Zeng, D. Huang, M. Cheng, L. Hu, W. Xiong, M. Chen, J. Wang, Semiconductor/boron nitride composites: synthesis, properties, and photocatalysis applications, Appl. Catal. B Environ. 238 (2018) 6–18.
[22] M. Zhu, Y. Osakada, S. Kim, M. Fujitsuka, T. Majima, Black phosphorus: a promising two dimensional visible and near-infrared-activated photocatalyst for hydrogen evolution, Appl. Catal. B Environ. 217 (2017) 285–292.
[23] X. Bai, C. Sun, D. Liu, X. Luo, D. Li, J. Wang, N. Wang, X. Chang, R. Zong, Y. Zhu, Photocatalytic degradation of deoxynivalenol using graphene/ZnO hybrids in aqueous suspension, Appl. Catal. B Environ. 204 (2017) 11–20.
[24] A. Navarro-Aguilar, S. Obregón, D. Hernández-Uresti, J. Suárez-de La Cruz, Effective coupling of $BiPO_4$/g-C_3N_4 hybrid composites in ciprofloxacin photodegradation, Res. Chem. Intermed. 45 (2019) 3865–3878.
[25] X. Wang, K. Maeda, A. Thomas, K. Takanabe, G. Xin, J.M. Carlsson, K. Domen, M. Antonietti, A metal-free polymeric photocatalyst for hydrogen production from water under visible light, Nat. Mater. 8 (2009) 76–80.
[26] Z. Jiang, W. Wan, H. Li, S. Yuan, H. Zhao, P.K. Wong, A hierarchical Z-scheme α-Fe_2O_3/g-C_3N_4 hybrid for enhanced photocatalytic CO_2 reduction, Adv. Mater. 30 (2018) 1706108.
[27] V.W. Lau, I. Moudrakovski, T. Botari, S. Weinberger, M.B. Mesch, V. Duppel, J. Senker, V. Blum, B.V. Lotsch, Rational design of carbon nitride photocatalysts by identification of cyanamide defects as catalytically relevant sites, Nat. Commun. 7 (2016) 1–10.
[28] L. Qin, G. Zeng, C. Lai, D. Huang, P. Xu, C. Zhang, M. Cheng, X. Liu, S. Liu, B. Li, "Gold rush" in modern science: fabrication strategies and typical advanced applications of gold nanoparticles in sensing, Coord. Chem. Rev. 359 (2018) 1–31.
[29] X. Wang, S. Blechert, M. Antonietti, Polymeric graphitic carbon nitride for heterogeneous photocatalysis, Acs Catal. 2 (2012) 1596–1606.
[30] Y. Wang, X. Wang, M. Antonietti, Polymeric graphitic carbon nitride as a heterogeneous organocatalyst: from photochemistry to multipurpose catalysis to sustainable chemistry, Angew. Chem. Int. Ed. 51 (2012) 68–89, https://doi.org/10.1002/anie.201101182.
[31] A. Du, S. Sanvito, Z. Li, D. Wang, Y. Jiao, T. Liao, Q. Sun, Y.H. Ng, Z. Zhu, R. Amal, Hybrid graphene and graphitic carbon nitride nanocomposite: gap opening, electron–hole puddle, interfacial charge transfer, and enhanced visible light response, J. Am. Chem. Soc. 134 (2012) 4393–4397.
[32] M.J. Lima, A.M. Silva, C.G. Silva, J.L. Faria, Graphitic carbon nitride modified by thermal, chemical and mechanical processes as metal-free photocatalyst for the selective synthesis of benzaldehyde from benzyl alcohol, J. Catal. 353 (2017) 44–53.
[33] F. Dong, L. Wu, Y. Sun, M. Fu, Z. Wu, S. Lee, Efficient synthesis of polymeric g-C_3N_4 layered materials as novel efficient visible light driven photocatalysts, J. Mater. Chem. 21 (2011) 15171–15174.

[34] S. Yan, Z. Li, Z. Zou, Photodegradation performance of g-C_3N_4 fabricated by directly heating melamine, Langmuir 25 (2009) 10397–10401.

[35] J. Zhang, F. Guo, X. Wang, An optimized and general synthetic strategy for fabrication of polymeric carbon nitride nanoarchitectures, Adv. Funct. Mater. 23 (2013) 3008–3014.

[36] A. Wang, C. Wang, L. Fu, W. Wong-Ng, Y. Lan, Recent advances of graphitic carbon nitride-based structures and applications in catalyst, sensing, imaging, and LEDs, Nano-Micro Lett. 9 (2017) 47, https://doi.org/10.1007/s40820-017-0148-2.

[37] J. Cermak, L. Kral, P. Roupcova, Improvement of hydrogen storage kinetics in ball-milled magnesium doped with antimony, Int. J. Hydrog. Energy. 42 (2017) 6144–6151.

[38] E. Jang, W.J. Kim, D.W. Kim, S.H. Hong, I. Ali, Y.M. Park, T.J. Park, Atomic layer deposition with rotary reactor for uniform hetero-junction photocatalyst, g-C_3N_4@ TiO_2 core–shell structures, RSC Adv. 9 (2019) 33180–33186.

[39] S. Tonda, S. Kumar, S. Kandula, V. Shanker, Fe-doped and-mediated graphitic carbon nitride nanosheets for enhanced photocatalytic performance under natural sunlight, J. Mater. Chem. A. 2 (2014) 6772–6780.

[40] J. Wu, S. Yang, J. Li, Y. Yang, G. Wang, X. Bu, P. He, J. Sun, J. Yang, Y. Deng, Electron injection of phosphorus doped g-C_3N_4 quantum dots: controllable photoluminescence emission wavelength in the whole visible light range with high quantum yield, Adv. Opt. Mater. 4 (2016) 2095–2101.

[41] J. Feng, H. Ma, T. Chen, C. Liu, Y. Ma, Passivated codoping can improve the solar-to-hydrogen efficiency of graphitic carbon nitride, J. Phys. Chem. C. 122 (2018) 7296–7302.

[42] W. Zhao, Y. Guo, S. Wang, H. He, C. Sun, S. Yang, A novel ternary plasmonic photocatalyst: ultrathin g-C_3N_4 nanosheet hybrided by Ag/$AgVO_3$ nanoribbons with enhanced visible-light photocatalytic performance, Appl. Catal. B Environ. 165 (2015) 335–343.

[43] Q. Gu, Y. Liao, L. Yin, J. Long, X. Wang, C. Xue, Template-free synthesis of porous graphitic carbon nitride microspheres for enhanced photocatalytic hydrogen generation with high stability, Appl. Catal. B Environ. 165 (2015) 503–510.

[44] X. Lu, K. Xu, P. Chen, K. Jia, S. Liu, C. Wu, Facile one step method realizing scalable production of g-C_3N_4 nanosheets and study of their photocatalytic H_2 evolution activity, (2014).

[45] P. Niu, L. Zhang, G. Liu, H. Cheng, Graphene-like carbon nitride nanosheets for improved photocatalytic activities, Adv. Funct. Mater. 22 (2012) 4763–4770.

[46] K. Schwinghammer, M.B. Mesch, V. Duppel, C. Ziegler, J. Senker, B.V. Lotsch, Crystalline carbon nitride nanosheets for improved visible-light hydrogen evolution, J. Am. Chem. Soc. 136 (2014) 1730–1733.

[47] M. Tahir, C. Cao, F.K. Butt, F. Idrees, N. Mahmood, Z. Ali, I. Aslam, M. Tanveer, M. Rizwan, T. Mahmood, Tubular graphitic-C_3N_4: a prospective material for energy storage and green photocatalysis, J. Mater. Chem. A. 1 (2013) 13949–13955.

[48] Y. Zheng, Z. Yu, H. Ou, A.M. Asiri, Y. Chen, X. Wang, Black phosphorus and polymeric carbon nitride heterostructure for photoinduced molecular oxygen activation, Adv. Funct. Mater. 28 (2018) 1705407.

[49] Y. Chen, W. Huang, D. He, Y. Situ, H. Huang, Construction of heterostructured g-C_3N_4/Ag/TiO_2 microspheres with enhanced photocatalysis performance under visible-light irradiation, ACS Appl. Mater. Interfaces. 6 (2014) 14405–14414.

[50] L. Ge, C. Han, J. Liu, In situ synthesis and enhanced visible light photocatalytic activities of novel PANI–g-C_3N_4 composite photocatalysts, J. Mater. Chem. 22 (2012) 11843–11850.

[51] S.-Z. Wu, K. Li, W.-D. Zhang, On the heterostructured photocatalysts Ag_3VO_4/g-C_3N_4 with enhanced visible light photocatalytic activity, Appl. Surf. Sci. 324 (2015) 324–331.

[52] H. Yan, Y. Huang, Polymer composites of carbon nitride and poly (3-hexylthiophene) to achieve enhanced hydrogen production from water under visible light, Chem. Commun. 47 (2011) 4168–4170.

[53] S. Zhang, J. Li, X. Wang, Y. Huang, M. Zeng, J. Xu, In situ ion exchange synthesis of strongly coupled Ag@AgCl/g-C_3N_4 porous nanosheets as plasmonic photocatalyst for highly efficient visible-light photocatalysis, ACS Appl. Mater. Interfaces. 6 (2014) 22116–22125.

[54] J. Liu, H. Xu, Y. Xu, Y. Song, J. Lian, Y. Zhao, L. Wang, L. Huang, H. Ji, H. Li, Graphene quantum dots modified mesoporous graphite carbon nitride with significant enhancement of photocatalytic activity, Appl. Catal. B Environ. 207 (2017) 429–437.

[55] Q. Sun, P. Wang, H. Yu, X. Wang, In situ hydrothermal synthesis and enhanced photocatalytic H_2-evolution performance of suspended rGO/g-C_3N_4 photocatalysts, J. Mol. Catal. Chem. 424 (2016) 369–376.

[56] Z. Tong, D. Yang, J. Shi, Y. Nan, Y. Sun, Z. Jiang, Three-dimensional porous aerogel constructed by g-C_3N_4 and graphene oxide nanosheets with excellent visible-light photocatalytic performance, ACS Appl. Mater. Interfaces. 7 (2015) 25693–25701.

[57] W. Wan, S. Yu, F. Dong, Q. Zhang, Y. Zhou, EfficientC_3N_4/graphene oxide macroscopic aerogel visible-light photocatalyst, J. Mater. Chem. A. 4 (2016) 7823–7829.

[58] N.S. Lewis, Research opportunities to advance solar energy utilization, Science 351 (2016).

[59] S.J. Lim, M.U. Zahid, P. Le, L. Ma, D. Entenberg, A.S. Harney, J. Condeelis, A. M. Smith, Brightness-equalized quantum dots, Nat. Commun. 6 (2015) 1–10.

[60] I.L. Medintz, M.H. Stewart, S.A. Trammell, K. Susumu, J.B. Delehanty, B.C. Mei, J.S. Melinger, J.B. Blanco-Canosa, P.E. Dawson, H. Mattoussi, Quantum-dot/dopamine bioconjugates function as redox coupled assemblies for in vitro and intracellular pH sensing, Nat. Mater. 9 (2010) 676–684.

[61] R. Abe, Recent progress on photocatalytic and photoelectrochemical water splitting under visible light irradiation, J. Photochem. Photobiol. C Photochem. Rev. 11 (2010) 179–209.

[62] S. Gao, L. Tang, J. Xiang, R. Ji, S.K. Lai, S. Yuan, S.P. Lau, Facile preparation of sulphur-doped graphene quantum dots for ultra-high performance ultraviolet photodetectors, New J. Chem. 41 (2017) 10447–10451.

[63] J. Wen, J. Xie, X. Chen, X. Li, A review on g-C_3N_4-based photocatalysts, Appl. Surf. Sci. 391 (2017) 72–123.

[64] X. Zou, Y. Zhang, Noble metal-free hydrogen evolution catalysts for water splitting, Chem. Soc. Rev. 44 (2015) 5148–5180.

[65] M.-H. Chan, R.-S. Liu, M. Hsiao, Graphitic carbon nitride-based nanocomposites and their biological applications: a review, Nanoscale 11 (2019) 14993–15003.

[66] S. Berardi, S. Drouet, L. Francàs, C. Gimbert-Suriñach, M. Guttentag, C. Richmond, T. Stoll, A. Llobet, Molecular artificial photosynthesis, Chem. Soc. Rev. 43 (2014) 7501–7519.

[67] J. Qin, H. Zeng, Photocatalysts fabricated by depositing plasmonic Ag nanoparticles on carbon quantum dots/graphitic carbon nitride for broad spectrum photocatalytic hydrogen generation, Appl. Catal. B Environ. 209 (2017) 161–173.

[68] F. Wang, P. Chen, Y. Feng, Z. Xie, Y. Liu, Y. Su, Q. Zhang, Y. Wang, K. Yao, W. Lv, Facile synthesis of N-doped carbon dots/g-C_3N_4 photocatalyst with enhanced visible-light photocatalytic activity for the degradation of indomethacin, Appl. Catal. B Environ. 207 (2017) 103–113.

[69] M.L. Cohen, Calculation of bulk moduli of diamond and zinc-blende solids, Phys. Rev. B. 32 (1985) 7988.

[70] J. Liebig, Uber einige Stickstoff-Verbindungen, Ann. Pharm. 10 (1834) 1–47.

[71] K. He, J. Xie, Z.-Q. Liu, N. Li, X. Chen, J. Hu, X. Li, Multi-functional Ni_3C cocatalyst/g-C_3N_4 nanoheterojunctions for robust photocatalytic H_2 evolution under visible light, J. Mater. Chem. A. 6 (2018) 13110–13122, https://doi.org/10.1039/C8TA03048K.

[72] J. Zhang, X. Mao, W. Xiao, Y. Zhuang, Photocatalytic degradation of sulfamethazine by graphitic carbon nitride-modified zinc molybdate: Effects of synthesis method on performance, degradation kinetics, and mechanism, Chin. J. Catal. 38 (2017) 2009–2020, https://doi.org/10.1016/S1872-2067(17)62935-8.

[73] M.Q. Wen, T. Xiong, Z.G. Zang, W. Wei, X.S. Tang, F. Dong, Synthesis of MoS_2/g-C_3N_4 nanocomposites with enhanced visible-light photocatalytic activity for the removal of nitric oxide (NO), Opt. Express. 24 (2016) 10205–10212, https://doi.org/10.1364/OE.24.010205.

[74] T.S. Anirudhan, J.R. Deepa, A.S. Nair, Fabrication of chemically modified graphene oxide/nano hydroxyapatite composite for adsorption and subsequent photocatalytic degradation of aureomycine hydrochloride, J. Ind. Eng. Chem. 47 (2017) 415–430, https://doi.org/10.1016/j.jiec.2016.12.014.

[75] W. Ho, Z. Zhang, M. Xu, X. Zhang, X. Wang, Y. Huang, Enhanced visible-light-driven photocatalytic removal of NO: Effect on layer distortion on g-C_3N_4 by H_2 heating, Appl. Catal. B Environ. 179 (2015) 106–112, https://doi.org/10.1016/j.apcatb.2015.05.010.

[76] X. Miao, X. Yue, Z. Ji, X. Shen, H. Zhou, M. Liu, K. Xu, J. Zhu, G. Zhu, L. Kong, S. A. Shah, Nitrogen-doped carbon dots decorated on g-C_3N_4/Ag_3PO_4 photocatalyst with improved visible light photocatalytic activity and mechanism insight, Appl. Catal. B Environ. 227 (2018) 459–469, https://doi.org/10.1016/j.apcatb.2018.01.057.

[77] X. Wang, K. Maeda, X. Chen, K. Takanabe, K. Domen, Y. Hou, X. Fu, M. Antonietti, Polymer semiconductors for artificial photosynthesis: hydrogen evolution by mesoporous graphitic carbon nitride with visible light, J. Am. Chem. Soc. 131 (2009) 1680–1681.

[78] F. Dong, Z. Wang, Y. Sun, W.-K. Ho, H. Zhang, Engineering the nanoarchitecture and texture of polymeric carbon nitride semiconductor for enhanced visible light photocatalytic activity, J. Colloid Interface Sci. 401 (2013) 70–79, https://doi.org/10.1016/j.jcis.2013.03.034.

[79] P. Yang, J. Zhao, W. Qiao, L. Li, Z. Zhu, Ammonia-induced robust photocatalytic hydrogen evolution of graphitic carbon nitride, Nanoscale 7 (2015) 18887–18890, https://doi.org/10.1039/C5NR05570A.

[80] H. Tong, B. Shi, S. Zhao, Facile synthesis of a direct Z-scheme BiOCl–phosphotungstic acid heterojunction for the improved photodegradation of tetracycline, RSC Adv. 10 (n.d.) 17369–17376. https://doi.org/10.1039/d0ra02396e.

[81] M. Zhou, Z. Hou, X. Chen, Graphitic-C_3N_4 nanosheets: synergistic effects of hydrogenation and n/n junctions for enhanced photocatalytic activities, Dalton Trans. 46 (2017) 10641–10649, https://doi.org/10.1039/C7DT00761B.

[82] F. Su, M. Antonietti, X. Wang, mpg-C_3N_4 as a solid base catalyst for Knoevenagel condensations and transesterification reactions, Catal Sci. Technol. 2 (2012) 1005–1009.

[83] W. Wang, C.Y. Jimmy, Z. Shen, D.K. Chan, T. Gu, g-C_3N_4 quantum dots: direct synthesis, upconversion properties and photocatalytic application, Chem. Commun. 50 (2014) 10148–10150.

[84] L. Maya, D.R. Cole, E.W. Hagaman, Carbon–nitrogen pyrolyzates: attempted preparation of carbon nitride, J. Am. Ceram. Soc. 74 (1991) 1686–1688.

[85] J. Zhou, Y. Yang, C. Zhang, A low-temperature solid-phase method to synthesize highly fluorescent carbon nitride dots with tunable emission, Chem. Commun. 49 (2013) 8605–8607.

[86] D.C. Nesting, J.V. Badding, High-pressure synthesis of sp^2-bonded carbon nitrides, Chem. Mater. 8 (1996) 1535–1539.

[87] J. Xu, H.-T. Wu, X. Wang, B. Xue, Y.-X. Li, Y. Cao, A new and environmentally benign precursor for the synthesis of mesoporous g-C_3N_4 with tunable surface area, Phys. Chem. Chem. Phys. 15 (2013) 4510–4517.

[88] D.R. Paul, R. Sharma, S. Nehra, A. Sharma, Effect of calcination temperature, pH and catalyst loading on photodegradation efficiency of urea derived graphitic carbon nitride towards methylene blue dye solution, RSC Adv. 9 (2019) 15381–15391.

[89] Y. Hong, C. Li, D. Li, Z. Fang, B. Luo, X. Yan, H. Shen, B. Mao, W. Shi, Precisely tunable thickness of graphitic carbon nitride nanosheets for visible-light-driven photocatalytic hydrogen evolution, Nanoscale 9 (2017) 14103–14110, https://doi.org/10.1039/C7NR05155G.

[90] T. Miller, A.B. Jorge, T. Suter, A. Sella, F. Cora, P. McMillan, Carbon nitrides: synthesis and characterization of a new class of functional materials, Phys. Chem. Chem. Phys. 19 (2017) 15613–15638.

[91] X. Chen, J. Zhang, X. Fu, M. Antonietti, X. Wang, Fe-g-C_3N_4-catalyzed oxidation of benzene to phenol using hydrogen peroxide and visible light, J. Am. Chem. Soc. 131 (2009) 11658–11659.

[92] X. Zou, Y. Yang, H. Chen, X.-L. Shi, S. Song, Z.-G. Chen, Hierarchical meso/macro-porous TiO_2/graphitic carbon nitride nanofibers with enhanced hydrogen evolution, Mater. Des. 202 (2021), 109542, https://doi.org/10.1016/j.matdes.2021.109542.

[93] U. Khan, A. O'Neill, M. Lotya, S. De, J.N. Coleman, High-concentration solvent exfoliation of graphene, Small Weinh. Bergstr. Ger. 6 (2010) 864–871, https://doi.org/10.1002/smll.200902066.

[94] Q. Lin, L. Li, S. Liang, M. Liu, J. Bi, L. Wu, Efficient synthesis of monolayer carbon nitride 2D nanosheet with tunable concentration and enhanced visible-light photocatalytic activities, Appl. Catal. B Environ. C (2015) 135–142, https://doi.org/10.1016/j.apcatb.2014.07.053.

[95] W. Wang, J.C. Yu, Z. Shen, D.K.L. Chan, T. Gu, g-C_3N_4 quantum dots: direct synthesis, upconversion properties and photocatalytic application, Chem. Commun. 50 (2014) 10148–10150, https://doi.org/10.1039/C4CC02543A.

[96] Direct conversion of urea into graphitic carbon nitride over mesoporous TiO_2 spheres under mild condition - Chemical Communications (RSC Publishing), (n.d.). https://pubs.rsc.org/en/content/articlelanding/2011/cc/c0cc03530k (accessed December 19, 2021).

[97] X.-X. Zou, G.-D. Li, Y.-N. Wang, J. Zhao, C. Yan, M.-Y. Guo, L. Li, J.-S. Chen, Direct conversion of urea into graphitic carbon nitride over mesoporous TiO_2 spheres under mild condition, Chem. Commun. 47 (2011) 1066–1068.

[98] Helical Graphitic Carbon Nitrides with Photocatalytic and Optical Activities - Zheng - 2014 - Angewandte Chemie International Edition - Wiley Online Library, (n.d.). https://onlinelibrary.wiley.com/doi/10.1002/anie.201407319 (accessed January 12, 2022).

[99] M. Ovcharov, N. Shcherban, S. Filonenko, A. Mishura, M. Skoryk, V. Shvalagin, V. Granchak, Hard template synthesis of porous carbon nitride materials with improved efficiency for photocatalytic CO_2 utilization, Mater. Sci. Eng. B. 202 (2015) 1–7, https://doi.org/10.1016/j.mseb.2015.08.003.

[100] S. Hwang, S. Lee, J.-S. Yu, Template-directed synthesis of highly ordered nanoporous graphitic carbon nitride through polymerization of cyanamide, Appl. Surf. Sci. 253 (2007) 5656–5659, https://doi.org/10.1016/j.apsusc.2006.12.032.

[101] A.J. Bard, Photoelectrochemistry and heterogeneous photo-catalysis at semiconductors, J. Photochem. 10 (1979) 59–75, https://doi.org/10.1016/0047-2670(79)80037-4.

[102] Q. Xu, L. Zhang, B. Cheng, J. Fan, J. Yu, S-scheme heterojunction photocatalyst, Chem 6 (2020) 1543–1559, https://doi.org/10.1016/j.chempr.2020.06.010.

[103] P. Zhou, J. Yu, M. Jaroniec, All-solid-state Z-scheme photocatalytic systems, Adv. Mater. 26 (2014) 4920–4935, https://doi.org/10.1002/adma.201400288.

[104] Q. Xu, L. Zhang, J. Yu, S. Wageh, A.A. Al-Ghamdi, M. Jaroniec, Direct Z-scheme photocatalysts: principles, synthesis, and applications, Mater. Today. 21 (2018) 1042–1063, https://doi.org/10.1016/j.mattod.2018.04.008.

[105] R.N. Baig, S. Verma, M.N. Nadagouda, R.S. Varma, Room temperature synthesis of biodiesel using sulfonated graphitic carbon nitride, Sci. Rep. 6 (2016) 1–6.

[106] A. Bayat, E. Saievar-Iranizad, Vertically aligned rutile TiO_2 nanorods sensitized with sulfur and nitrogen co-doped graphene quantum dots for water splitting: an energy level study, J. Alloys Compd. 755 (2018) 192–198.

[107] S. Asadzadeh-Khaneghah, A. Habibi-Yangjeh, D. Seifzadeh, Graphitic carbon nitride nanosheets coupled with carbon dots and BiOI nanoparticles: boosting visible-light-driven photocatalytic activity, J. Taiwan Inst. Chem. Eng. 87 (2018) 98–111.

[108] Q. Han, F. Zhao, C. Hu, L. Lv, Z. Zhang, N. Chen, L. Qu, Facile production of ultrathin graphitic carbon nitride nanoplatelets for efficient visible-light water splitting, Nano Res. 8 (2015) 1718–1728.

[109] L. Wang, Y. Hong, E. Liu, Z. Wang, J. Chen, S. Yang, J. Wang, X. Lin, J. Shi, Rapid polymerization synthesizing high-crystalline g-C_3N_4 towards boosting solar photocatalytic H_2 generation, Int. J. Hydrog. Energy. 45 (2020) 6425–6436.

[110] W.-K. Jo, T. Adinaveen, J.J. Vijaya, N.C.S. Selvam, Synthesis of MoS_2 nanosheet supported Z-scheme TiO_2/g-C_3N_4 photocatalysts for the enhanced photocatalytic degradation of organic water pollutants, Rsc Adv. 6 (2016) 10487–10497.

[111] W. Chen, Z.-C. He, G.-B. Huang, C.-L. Wu, W.-F. Chen, X.-H. Liu, Direct Z-scheme 2D/2D $MnIn_2S_4$/g-C_3N_4 architectures with highly efficient photocatalytic activities towards treatment of pharmaceutical wastewater and hydrogen evolution, Chem. Eng. J. 359 (2019) 244–253.

[112] Q. Qiao, K. Yang, L.-L. Ma, W.-Q. Huang, B.-X. Zhou, A. Pan, W. Hu, X. Fan, G.-F. Huang, Facile in situ construction of mediator-free direct Z-scheme g-C_3N_4/CeO_2 heterojunctions with highly efficient photocatalytic activity, J. Phys. Appl. Phys. 51 (2018), 275302.

[113] R. Ye, H. Fang, Y.-Z. Zheng, N. Li, Y. Wang, X. Tao, Fabrication of $CoTiO_3$/g-C_3N_4 hybrid photocatalysts with enhanced H_2 evolution: Z-scheme photocatalytic mechanism insight, ACS Appl. Mater. Interfaces. 8 (2016) 13879–13889.

[114] H. Katsumata, Y. Tachi, T. Suzuki, S. Kaneco, Z-scheme photocatalytic hydrogen production over WO_3/g-C_3N_4 composite photocatalysts, RSC Adv. 4 (2014) 21405–21409.

[115] S. Samanta, S. Martha, K. Parida, Facile synthesis of Au/g-C_3N_4 nanocomposites: an inorganic/organic hybrid plasmonic photocatalyst with enhanced hydrogen gas evolution under visible-light irradiation, ChemCatChem 6 (2014) 1453–1462.

[116] M. Caux, F. Fina, J.T. Irvine, H. Idriss, R. Howe, Impact of the annealing temperature on Pt/g-C_3N_4 structure, activity and selectivity between photodegradation and water splitting, Catal. Today. 287 (2017) 182–188.

[117] Y. Zhang, D.M. Ligthart, X.-Y. Quek, L. Gao, E.J. Hensen, Influence of Rh nanoparticle size and composition on the photocatalytic water splitting performance of Rh/graphitic carbon nitride, Int. J. Hydrog. Energy. 39 (2014) 11537–11546.

[118] J. Yu, S. Wang, B. Cheng, Z. Lin, F. Huang, Noble metal-free Ni $(OH)_2$–g-C_3N_4 composite photocatalyst with enhanced visible-light photocatalytic H_2-production activity, Catal, Sci. Technol. 3 (2013) 1782–1789.

[119] J. Qin, J. Huo, P. Zhang, J. Zeng, T. Wang, H. Zeng, Improving the photocatalytic hydrogen production of Ag/g-C_3N_4 nanocomposites by dye-sensitization under visible light irradiation, Nanoscale 8 (2016) 2249–2259.

[120] X.-B. Qian, W. Peng, J.-H. Huang, Fluorescein-sensitized Au/g-C_3N_4 nanocomposite for enhanced photocatalytic hydrogen evolution under visible light, Mater. Res. Bull. 102 (2018) 362–368.

[121] X. Li, X. Lv, N. Li, J. Wu, Y.-Z. Zheng, X. Tao, One-step hydrothermal synthesis of high-percentage 1T-phase MoS_2 quantum dots for remarkably enhanced visible-light-driven photocatalytic H_2 evolution, Appl. Catal. B Environ. 243 (2019) 76–85.

[122] P.-W. Chen, K. Li, Y.-X. Yu, W.-D. Zhang, Cobalt-doped graphitic carbon nitride photocatalysts with high activity for hydrogen evolution, Appl. Surf. Sci. 392 (2017) 608–615.

[123] Y.-P. Zhu, T.-Z. Ren, Z.-Y. Yuan, Mesoporous phosphorus-doped g-C_3N_4 nanostructured flowers with superior photocatalytic hydrogen evolution performance, ACS Appl. Mater. Interfaces. 7 (2015) 16850–16856.

[124] J. Ran, T.Y. Ma, G. Gao, X.-W. Du, S.Z. Qiao, Porous P-doped graphitic carbon nitride nanosheets for synergistically enhanced visible-light photocatalytic H_2 production, Energy Environ. Sci. 8 (2015) 3708–3717.

[125] Y. Zhou, L. Zhang, J. Liu, X. Fan, B. Wang, M. Wang, W. Ren, J. Wang, M. Li, J. Shi, Brand new P-doped g-CN_4. Enhanced Photocatalytic Activity for H_2 Evolution and Rhodamine B Degradation Under VisiBle Light, 2015.

[126] S. Guo, Z. Deng, M. Li, B. Jiang, C. Tian, Q. Pan, H. Fu, Phosphorus-doped carbon nitride tubes with a layered micro-nanostructure for enhanced visible-light photocatalytic hydrogen evolution, Angew. Chem. 128 (2016) 1862–1866.

[127] G. Liu, P. Niu, C. Sun, S.C. Smith, Z. Chen, G.Q. Lu, H.-M. Cheng, Unique electronic structure induced high photoreactivity of sulfur-doped graphitic C_3N_4, J. Am. Chem. Soc. 132 (2010) 11642–11648.

[128] L. Ge, C. Han, X. Xiao, L. Guo, Y. Li, Enhanced visible light photocatalytic hydrogen evolution of sulfur-doped polymeric g-C_3N_4 photocatalysts, Mater. Res. Bull. 48 (2013) 3919–3925.

[129] J. Hong, X. Xia, Y. Wang, R. Xu, Mesoporous carbon nitride with in situ sulfur doping for enhanced photocatalytic hydrogen evolution from water under visible light, J. Mater. Chem. 22 (2012) 15006–15012.

[130] J. Li, B. Shen, Z. Hong, B. Lin, B. Gao, Y. Chen, A facile approach to synthesize novel oxygen-doped g-C_3N_4 with superior visible-light photoreactivity, Chem. Commun. 48 (2012) 12017–12019.

[131] Z.-F. Huang, J. Song, L. Pan, Z. Wang, X. Zhang, J.-J. Zou, W. Mi, X. Zhang, L. Wang, Carbon nitride with simultaneous porous network and O-doping for efficient solar-energy-driven hydrogen evolution, Nano Energy 12 (2015) 646–656.

[132] X. She, L. Liu, H. Ji, Z. Mo, Y. Li, L. Huang, D. Du, H. Xu, H. Li, Template-free synthesis of 2D porous ultrathin nonmetal-doped g-C_3N_4 nanosheets with highly efficient photocatalytic H_2 evolution from water under visible light, Appl. Catal. B Environ. 187 (2016) 144–153.

[133] S. Guo, Y. Zhu, Y. Yan, Y. Min, J. Fan, Q. Xu, Holey structured graphitic carbon nitride thin sheets with edge oxygen doping via photo-Fenton reaction with enhanced photocatalytic activity, Appl. Catal. B Environ. 185 (2016) 315–321.

[134] Z. Lin, X. Wang, Nanostructure engineering and doping of conjugated carbon nitride semiconductors for hydrogen photosynthesis, Angew. Chem. 125 (2013) 1779–1782.

[135] Y. Wang, Y. Di, M. Antonietti, H. Li, X. Chen, X. Wang, Excellent visible-light photocatalysis of fluorinated polymeric carbon nitride solids, Chem. Mater. 22 (2010) 5119–5121.

[136] G. Zhang, M. Zhang, X. Ye, X. Qiu, S. Lin, X. Wang, Iodine modified carbon nitride semiconductors as visible light photocatalysts for hydrogen evolution, Adv. Mater. 26 (2014) 805–809.

[137] Q. Han, C. Hu, F. Zhao, Z. Zhang, N. Chen, L. Qu, One-step preparation of iodine-doped graphitic carbon nitride nanosheets as efficient photocatalysts for visible light water splitting, J. Mater. Chem. A. 3 (2015) 4612–4619.

[138] Z.-A. Lan, G. Zhang, X. Wang, A facile synthesis of Br-modified g-C_3N_4 semiconductors for photoredox water splitting, Appl. Catal. B Environ. 192 (2016) 116–125.

[139] Z. Jin, X. Jiang, Q. Zhang, S. Huang, L. Zhang, L. Huang, T. He, H. Zhang, T. Ohno, S. Ruan, Infrared response in photocatalytic polymeric carbon nitride for water splitting via an upconversion mechanism, Commun. Mater. 1 (2020) 1–10.

[140] Y. Li, W. Ho, K. Lv, B. Zhu, S.C. Lee, Carbon vacancy-induced enhancement of the visible light-driven photocatalytic oxidation of NO over g-C_3N_4 nanosheets, Appl. Surf. Sci. 430 (2018) 380–389.

[141] Q. Liang, Z. Li, Z. Huang, F. Kang, Q. Yang, Holey graphitic carbon nitride nanosheets with carbon vacancies for highly improved photocatalytic hydrogen production, Adv. Funct. Mater. 25 (2015) 6885–6892.

[142] S. Liu, J. Ke, H. Sun, J. Liu, M.O. Tade, S. Wang, Size dependence of uniformed carbon spheres in promoting graphitic carbon nitride toward enhanced photocatalysis, Appl. Catal. B Environ. 204 (2017) 358–364.

[143] R.C. Pawar, S. Kang, J.H. Park, J. Kim, S. Ahn, C.S. Lee, Room-temperature synthesis of nanoporous 1D microrods of graphitic carbon nitride (g-C_3N_4) with highly enhanced photocatalytic activity and stability, Sci. Rep. 6 (2016) 1–14.

[144] C. Pu, J. Wan, E. Liu, Y. Yin, J. Li, Y. Ma, J. Fan, X. Hu, Two-dimensional porous architecture of protonated GCN and reduced graphene oxide via electrostatic self-assembly strategy for high photocatalytic hydrogen evolution under visible light, Appl. Surf. Sci. 399 (2017) 139–150.

[145] J. Rashid, N. Parveen, A. Iqbal, S.U. Awan, N. Iqbal, S.H. Talib, N. Hussain, B. Akram, A. Ulhaq, B. Ahmed, Facile synthesis of g-C_3N_4 (0.94)/CeO_2 (0.05)/Fe_3O_4 (0.01) nanosheets for DFT supported visible photocatalysis of 2-Chlorophenol, Sci. Rep. 9 (2019) 1–14.

[146] M. Tahir, N. Mahmood, J. Zhu, A. Mahmood, F.K. Butt, S. Rizwan, I. Aslam, M. Tanveer, F. Idrees, I. Shakir, One dimensional graphitic carbon nitrides as effective metal-free oxygen reduction catalysts, Sci. Rep. 5 (2015) 1–10.

[147] X. Wang, M. Hong, F. Zhang, Z. Zhuang, Y. Yu, Recyclable nanoscale zero valent iron doped g-C_3N_4/MoS_2 for efficient photocatalysis of RhB and Cr (VI) driven by visible light, ACS Sustain. Chem. Eng. 4 (2016) 4055–4063.

[148] C. Xu, S. Wu, G. Xiong, X. Guo, H. Yang, J. Yan, K. Cen, Z. Bo, K.K. Ostrikov, Nanoconfined fusion of g-C_3N_4 within edge-rich vertically oriented graphene hierarchical networks for high-performance photocatalytic hydrogen evolution utilizing superhydrophillic and superaerophobic responses in seawater, Appl. Catal. B Environ. 280 (2021), 119461.

[149] T. Robinson, G. McMullan, R. Marchant, P. Nigam, Remediation of dyes in textile effluent: a critical review on current treatment technologies with a proposed alternative, Bioresour. Technol. 77 (2001) 247–255.

[150] R.G. Saratale, G.D. Saratale, J.-S. Chang, S. Govindwar, Bacterial decolorization and degradation of azo dyes: a review, J. Taiwan Inst. Chem. Eng. 42 (2011) 138–157.

[151] F. Yu, L. Wang, Q. Xing, D. Wang, X. Jiang, G. Li, A. Zheng, F. Ai, J.-P. Zou, Functional groups to modify g-C_3N_4 for improved photocatalytic activity of hydrogen evolution from water splitting, Chin. Chem. Lett. 31 (2020) 1648–1653.

[152] Y. Zheng, J. Liu, J. Liang, M. Jaroniec, S.Z. Qiao, Graphitic carbon nitride materials: controllable synthesis and applications in fuel cells and photocatalysis, Energy Environ. Sci. 5 (2012) 6717–6731.

[153] Y. Wang, X. Wang, M. Antonietti, Y. Zhang, Facile one-pot synthesis of nanoporous carbon nitride solids by using soft templates, ChemSusChem Chem. Sustain. Energy Mater. 3 (2010) 435–439.

[154] S. Kumar, T. Surendar, A. Baruah, V. Shanker, Synthesis of a novel and stable g-C_3N_4–Ag_3PO_4 hybrid nanocomposite photocatalyst and study of the photocatalytic activity under visible light irradiation, J. Mater. Chem. A. 1 (2013) 5333–5340.

[155] X. Wang, J. Cheng, H. Yu, J. Yu, A facile hydrothermal synthesis of carbon dots modified g-C_3N_4 for enhanced photocatalytic H_2-evolution performance, Dalton Trans. 46 (2017) 6417–6424.

[156] Q. Liu, T. Chen, Y. Guo, Z. Zhang, X. Fang, Ultrathin g-C_3N_4 nanosheets coupled with carbon nanodots as 2D/0D composites for efficient photocatalytic H_2 evolution, Appl. Catal. B Environ. 193 (2016) 248–258.

[157] Y. Wang, X. Liu, J. Liu, B. Han, X. Hu, F. Yang, Z. Xu, Y. Li, S. Jia, Z. Li, Carbon quantum dot implanted graphite carbon nitride nanotubes: excellent charge separation and enhanced photocatalytic hydrogen evolution, Angew. Chem. 130 (2018) 5867–5873.

[158] K. Wang, X. Wang, H. Pan, Y. Liu, S. Xu, S. Cao, In situ fabrication of CDs/g-C_3N_4 hybrids with enhanced interface connection via calcination of the precursors for photocatalytic H_2 evolution, Int. J. Hydrog. Energy. 43 (2018) 91–99.

[159] X.-H. Jiang, L.-C. Wang, F. Yu, Y.-C. Nie, Q.-J. Xing, X. Liu, Y. Pei, J.-P. Zou, W.-L. Dai, Photodegradation of organic pollutants coupled with simultaneous photocatalytic evolution of hydrogen using quantum-dot-modified g-C_3N_4 catalysts under visible-light irradiation, ACS Sustain. Chem. Eng. 6 (2018) 12695–12705.

[160] Y. Li, X. Feng, Z. Lu, H. Yin, F. Liu, Q. Xiang, Enhanced photocatalytic H_2-production activity of C-dots modified g-C_3N_4/TiO_2 nanosheets composites, J. Colloid Interface Sci. 513 (2018) 866–876.

[161] Y. Wang, Y. Li, J. Zhao, J. Wang, Z. Li, g-C_3N_4/B doped g-C_3N_4 quantum dots heterojunction photocatalysts for hydrogen evolution under visible light, Int. J. Hydrog. Energy. 44 (2019) 618–628.

[162] H. Wang, X. Yuan, H. Wang, X. Chen, Z. Wu, L. Jiang, W. Xiong, G. Zeng, Facile synthesis of Sb_2S_3/ultrathin g-C_3N_4 sheets heterostructures embedded with g-C_3N_4 quantum dots with enhanced NIR-light photocatalytic performance, Appl. Catal. B Environ. 193 (2016) 36–46.

[163] P. Chen, P. Xing, Z. Chen, X. Hu, H. Lin, L. Zhao, Y. He, In-situ synthesis of $AgNbO_3$/g-C_3N_4 photocatalyst via microwave heating method for efficiently photocatalytic H_2 generation, J. Colloid Interface Sci. 534 (2019) 163–171.

[164] T. Silva Veras, T.S. Mozer, A. Silva César, Hydrogen: trends, production and characterization of the main process worldwide, Int. J. Hydrog. Energy. 42 (2017) 2018–2033.

[165] M. Wang, M. Ye, J. Iocozzia, Z. Lin, Photocatalytic Hydrogen Generation Enabled by Nanostructured TiO, Hydrog, Prod. Technol. (2017) 545.

[166] X. Chen, S. Shen, L. Guo, S.S. Mao, Semiconductor-based photocatalytic hydrogen generation, Chem. Rev. 110 (2010) 6503–6570.

[167] S.E. Hosseini, M.A. Wahid, Hydrogen production from renewable and sustainable energy resources: promising green energy carrier for clean development, Renew. Sustain. Energy Rev. 57 (2016) 850–866.

[168] S.S. Mao, X. Chen, Selected nanotechnologies for renewable energy applications, Int. J. Energy Res. 31 (2007) 619–636.

[169] A. Fujishima, K. Honda, Electrochemical photolysis of water at a semiconductor electrode, Nature 238 (1972) 37–38.

[170] R.M. Navarro Yerga, M.C. Alvarez Galvan, F. Del Valle, J.A. Villoria de la Mano, J. L. Fierro, Water splitting on semiconductor catalysts under visible-light irradiation, ChemSusChem Chem. Sustain. Energy Mater. 2 (2009) 471–485.

[171] A. Kudo, Recent progress in the development of visible light-driven powdered photocatalysts for water splitting, Int. J. Hydrog. Energy. 32 (2007) 2673–2678.

[172] F. Jiang, T. Yan, H. Chen, A. Sun, C. Xu, X. Wang, A g-C_3N_4–CdS composite catalyst with high visible-light-driven catalytic activity and photostability for methylene blue degradation, Appl. Surf. Sci. 295 (2014) 164–172.

[173] A. Naseri, M. Samadi, A. Pourjavadi, A.Z. Moshfegh, S. Ramakrishna, Graphitic carbon nitride (g-C_3N_4)-based photocatalysts for solar hydrogen generation: recent advances and future development directions, J. Mater. Chem. A. 5 (2017) 23406–23433.

[174] C. Feng, Y. Deng, L. Tang, G. Zeng, J. Wang, J. Yu, Y. Liu, B. Peng, H. Feng, J. Wang, Core-shell Ag_2CrO_4/N-GQDs@g-C_3N_4 composites with anti-photocorrosion performance for enhanced full-spectrum-light photocatalytic activities, Appl. Catal. B Environ. 239 (2018) 525–536.

[175] R. Ranjithkumar, P. Lakshmanan, P. Devendran, N. Nallamuthu, S. Sudhahar, M. K. Kumar, Investigations on effect of graphitic carbon nitride loading on the properties and electrochemical performance of g-C_3N_4/TiO_2 nanocomposites for energy storage device applications, Mater. Sci. Semicond. Process. 121 (2021), 105328.

[176] Y. Tian, L. Zhou, Q. Zhu, J. Lei, L. Wang, J. Zhang, Y. Liu, Hierarchical macro-mesoporous g-C_3N_4 with an inverse opal structure and vacancies for high-efficiency solar energy conversion and environmental remediation, Nanoscale 11 (2019) 20638–20647.

[177] A. Boudjemaa, I. Popescu, T. Juzsakova, M. Kebir, N. Helaili, K. Bachari, I.-C. Marcu, M-substituted (M = Co, Ni and Cu) zinc ferrite photo-catalysts for hydrogen production by water photo-reduction, Int. J. Hydrog. Energy. 41 (2016) 11108–11118.

[178] F. Fresno, T. Yoshida, N. Gokon, R. Fernández-Saavedra, T. Kodama, Comparative study of the activity of nickel ferrites for solar hydrogen production by two-step thermochemical cycles, Int. J. Hydrog. Energy. 35 (2010) 8503–8510.

[179] Z. Wei, F. Liang, Y. Liu, W. Luo, J. Wang, W. Yao, Y. Zhu, Photoelectrocatalytic degradation of phenol-containing wastewater by TiO_2/g-C_3N_4 hybrid heterostructure thin film, Appl. Catal. B Environ. 201 (2017) 600–606.

[180] C. Miranda, H. Mansilla, J. Yáñez, S. Obregón, G. Colón, Improved photocatalytic activity of g-C_3N_4/TiO_2 composites prepared by a simple impregnation method, J. Photochem. Photobiol. Chem. 253 (2013) 16–21.

[181] M. Wu, J.-M. Yan, X.-W. Zhang, M. Zhao, Q. Jiang, Ag_2O modified g-C_3N_4 for highly efficient photocatalytic hydrogen generation under visible light irradiation, J. Mater. Chem. A. 3 (2015) 15710–15714, https://doi.org/10.1039/C5TA03358F.

[182] Facile Fabrication of Highly Efficient g-C_3N_4/Ag_2O Heterostructured Photocatalysts with Enhanced Visible-Light Photocatalytic Activity | ACS Applied Materials & Interfaces, (n.d.). https://pubs.acs.org/doi/full/10.1021/am4038307 (accessed January 13, 2022).

[183] Ag_2O as a New Visible-Light Photocatalyst: Self-Stability and High Photocatalytic Activity - Wang - 2011 - Chemistry – A European Journal - Wiley Online Library, (n.d.). https://chemistry-europe.onlinelibrary.wiley.com/doi/10.1002/chem.201101032 (accessed January 13, 2022).

[184] R. Sun, Q. Shi, M. Zhang, L. Xie, J. Chen, X. Yang, M. Chen, W. Zhao, Enhanced photocatalytic oxidation of toluene with a coral-like direct Z-scheme $BiVO_4$/g-C_3N_4 photocatalyst, J. Alloys Compd. 714 (2017) 619–626.

[185] Y. Wang, L. Bai, Z. Zhang, Y. Qu, L. Jing, Improved visible-light photoactivity of Pt/g-C_3N_4 nanosheets for solar fuel production via pretreated boric acid modification, Res. Chem. Intermed. 45 (2019) 249–259.

[186] P. Xia, B. Zhu, B. Cheng, J. Yu, J. Xu, 2D/2D g-C_3N_4/MnO_2 nanocomposite as a direct Z-scheme photocatalyst for enhanced photocatalytic activity, ACS Sustain. Chem. Eng. 6 (2018) 965–973, https://doi.org/10.1021/acssuschemeng.7b03289.

[187] W. Gu, F. Lu, C. Wang, S. Kuga, L. Wu, Y. Huang, M. Wu, Face-to-face interfacial assembly of ultrathin g-C_3N_4 and anatase TiO_2 nanosheets for enhanced solar photocatalytic activity, ACS Appl. Mater. Interfaces. 9 (2017) 28674–28684, https://doi.org/10.1021/acsami.7b10010.

[188] Z. Sun, Z. Yu, Y. Liu, C. Shi, M. Zhu, A. Wang, Construction of 2D/2D $BiVO_4$/g-C_3N_4 nanosheet heterostructures with improved photocatalytic activity, J. Colloid Interface Sci. 533 (2019) 251–258, https://doi.org/10.1016/j.jcis.2018.08.071.

[189] J. Yu, S. Wang, J. Low, W. Xiao, Enhanced photocatalytic performance of direct Z-scheme g-C_3N_4–TiO_2 photocatalysts for the decomposition of formaldehyde in air, Phys. Chem. Chem. Phys. 15 (2013) 16883–16890, https://doi.org/10.1039/C3CP53131G.

[190] J. Jia, W. Sun, Q. Zhang, X. Zhang, X. Hu, E. Liu, J. Fan, Inter-plane heterojunctions within 2D/2D $FeSe_2$/g-C_3N_4 nanosheet semiconductors for photocatalytic hydrogen generation, Appl. Catal. B Environ. 261 (2020), 118249, https://doi.org/10.1016/j.apcatb.2019.118249.

[191] M. Zhou, G. Dong, F. Yu, Y. Huang, The deep oxidation of NO was realized by Sr multi-site doped g-C_3N_4 via photocatalytic method, Appl. Catal. B Environ. 256 (2019), 117825.

[192] P. Matheswaran, P. Thangavelu, B. Palanivel, Carbon dot sensitized integrative g-C_3N_4/AgCl Hybrids: A synergetic interaction for enhanced visible light driven photocatalytic process, Adv. Powder Technol. 30 (2019) 1715–1723, https://doi.org/10.1016/j.apt.2019.05.024.

[193] A. Azhar, M.A. Basit, W. Mehmood, M.A. Ali, S. Zahid, M. Ahmad, S.J.A. Zaidi, T. J. Park, Synchronized wet-chemical development of 2-dimensional MoS_2 and g-C_3N_4/MoS_2 QDs nanocomposite as efficient photocatalysts for detoxification of aqueous dye solutions, Colloids Surf. Physicochem. Eng. Asp. 657 (2023), 130581, https://doi.org/10.1016/j.colsurfa.2022.130581.

[194] S. Zahid, Z. Tariq, A. Azhar, S.U. Khan, U. Ali, M.A. Basit, Electroanalytical investigation of quantum-dot based deposition of metal chalcogenides on g-C_3N_4 for improved photochemical performance, Colloids Surf. Physicochem. Eng. Asp. 645 (2022), 128905, https://doi.org/10.1016/j.colsurfa.2022.128905.

[195] E. Jang, D.W. Kim, S.H. Hong, Y.M. Park, T.J. Park, Visible light-driven g-C_3N_4@ ZnO heterojunction photocatalyst synthesized via atomic layer deposition with a specially designed rotary reactor, Appl. Surf. Sci. 487 (2019) 206–210, https://doi.org/10.1016/j.apsusc.2019.05.035.

[196] Q. Zhu, B. Qiu, H. Duan, Y. Gong, Z. Qin, B. Shen, M. Xing, J. Zhang, Electron directed migration cooperated with thermodynamic regulation over bimetallic NiFeP/g-C_3N_4 for enhanced photocatalytic hydrogen evolution, Appl. Catal. B Environ. 259 (2019), 118078.

[197] Y. Peng, B. Lu, L. Chen, N. Wang, J.E. Lu, Y. Ping, S. Chen, Hydrogen evolution reaction catalyzed by ruthenium ion-complexed graphitic carbon nitride nanosheets, J. Mater. Chem. A. 5 (2017) 18261–18269.

[198] S. Riyajuddin, S. Tarik Aziz, S. Kumar, G.D. Nessim, K. Ghosh, 3D-graphene decorated with g-C_3N_4/Cu_3P composite: a noble metal-free bifunctional electrocatalyst for overall water splitting, ChemCatChem 12 (2020) 1394–1402.

[199] Z. Qin, M. Wang, R. Li, Y. Chen, Novel Cu_3P/g-C_3N_4 p-n heterojunction photocatalysts for solar hydrogen generation, Sci. China Mater. 61 (2018) 861–868.

[200] H. Li, Y. Wu, C. Li, Y. Gong, L. Niu, X. Liu, Q. Jiang, C. Sun, S. Xu, Design of Pt/t-ZrO_2/g-C_3N_4 efficient photocatalyst for the hydrogen evolution reaction, Appl. Catal. B Environ. 251 (2019) 305–312.

[201] X. Han, D. Xu, L. An, C. Hou, Y. Li, Q. Zhang, H. Wang, WO_3/g-C_3N_4 two-dimensional composites for visible-light driven photocatalytic hydrogen production, Int. J. Hydrog. Energy. 43 (2018) 4845–4855.

[202] H. Zhao, H. Zhang, G. Cui, Y. Dong, G. Wang, P. Jiang, X. Wu, N. Zhao, A photochemical synthesis route to typical transition metal sulfides as highly efficient cocatalyst for hydrogen evolution: from the case of NiS/g-C_3N_4, Appl. Catal. B Environ. 225 (2018) 284–290.

[203] H. Gao, Y. Liu, L. Wang, J. Zhu, S. Gao, X. Xia, Synthesis of a reticular porous MoS 2/g-C_3N_4 heterojunction with enhanced visible light efficiency in photocatalytic degradation of RhB, Res. Chem. Intermed. 45 (2019) 3687–3703.

[204] X.-L. Luo, G.-L. He, Y.-P. Fang, Y.-H. Xu, Nickel sulfide/graphitic carbon nitride/strontium titanate (NiS/g-C_3N_4/$SrTiO_3$) composites with significantly enhanced photocatalytic hydrogen production activity, J. Colloid Interface Sci. 518 (2018) 184–191.

[205] J. Li, Q. Xing, Y. Zhou, H. Huang, F. Dong, The activation of reactants and intermediates promotes the selective photocatalytic NO conversion on electron-localized Sr-intercalated g-C_3N_4, Appl. Catal. B Environ. 232 (2018) 69–76.

[206] Z. Chen, P. Sun, B. Fan, Z. Zhang, X. Fang, In situ template-free ion-exchange process to prepare visible-light-active g-C_3N_4/NiS hybrid photocatalysts with enhanced hydrogen evolution activity, J. Phys. Chem. C. 118 (2014) 7801–7807, https://doi.org/10.1021/jp5000232.

[207] T. Ajeesha, A. Ashwini, M. George, M. Teresita, Photocatalytic degradation of organic pollutant using Copper substituted calcium ferrite, Int. J. Res. Appl. Sci. Eng. Technol. 6 (2018) 3288–3297.

[208] A. Baban, A. Yediler, N.K. Ciliz, Integrated water management and CP implementation for wool and textile blend processes, CLEAN–Soil Air Water. 38 (2010) 84–90.

[209] K. Pamecha, V. Mehta, B. Kabra, Photocatalytic degradation of commercial textile Azo Dye Reactive Blue 160 by heterogeneous photocatalysis, Adv Appl Sci Res. 7 (2016) 95–101.

[210] E. Bizani, K. Fytianos, I. Poulios, V. Tsiridis, Photocatalytic decolorization and degradation of dye solutions and wastewaters in the presence of titanium dioxide, J. Hazard. Mater. 136 (2006) 85–94.

[211] S.-M. Lam, J.-C. Sin, A.R. Mohamed, A review on photocatalytic application of g-C_3N_4/semiconductor (CNS) nanocomposites towards the erasure of dyeing wastewater, Mater. Sci. Semicond. Process. 47 (2016) 62–84.

[212] N.P. Xekoukoulotakis, N. Xinidis, M. Chroni, D. Mantzavinos, D. Venieri, E. Hapeshi, D. Fatta-Kassinos, UV-A/TiO_2 photocatalytic decomposition of erythromycin in water: Factors affecting mineralization and antibiotic activity, Catal. Today. 151 (2010) 29–33.

[213] W. Zhang, K. Bhattacharya, A computational model of ferroelectric domains. Part II: grain boundaries and defect pinning, Acta Mater. 53 (2005) 199–209.

[214] R.A. Pawar, D.R. Shinde, P.S. Tambade, Synthesis of ZnO photocatalyst via ZnO_2 precursor and its application for dye degradation from effluent under solar irradiation, Desalination Water Treat. 57 (2016) 16514–16521.

[215] I. Udom, M.K. Ram, E.K. Stefanakos, A.F. Hepp, D.Y. Goswami, One dimensional-ZnO nanostructures: Synthesis, properties and environmental applications, Mater. Sci. Semicond. Process. 16 (2013) 2070–2083.

[216] C. Yang, W. Dong, G. Cui, Y. Zhao, X. Shi, X. Xia, B. Tang, W. Wang, Highly efficient photocatalytic degradation of methylene blue by P2ABSA-modified TiO_2 nanocomposite due to the photosensitization synergetic effect of TiO_2 and P2ABSA, RSC Adv. 7 (2017) 23699–23708.

[217] C. Crowell, S. Sze, Current transport in metal-semiconductor barriers, Solid-State Electron. 9 (1966) 1035–1048.

[218] L. Ye, J. Liu, Z. Jiang, T. Peng, L. Zan, Facets coupling of BiOBr-g-C_3N_4 composite photocatalyst for enhanced visible-light-driven photocatalytic activity, Appl. Catal. B Environ. 142 (2013) 1–7.

[219] D. Jiang, L. Chen, J. Zhu, M. Chen, W. Shi, J. Xie, Novel p–n heterojunction photocatalyst constructed by porous graphite-like C_3N_4 and nanostructured BiOI: facile synthesis and enhanced photocatalytic activity, Dalton Trans. 42 (2013) 15726–15734.

[220] X. Wang, Q. Wang, F. Li, W. Yang, Y. Zhao, Y. Hao, S. Liu, Novel BiOCl–C_3N_4 heterojunction photocatalysts: in situ preparation via an ionic-liquid-assisted solvent-thermal route and their visible-light photocatalytic activities, Chem. Eng. J. 234 (2013) 361–371.

[221] Y. Wang, X. Bai, C. Pan, J. He, Y. Zhu, Enhancement of photocatalytic activity of Bi_2 WO_6 hybridized with graphite-like C_3N_4, J. Mater. Chem. 22 (2012) 11568–11573.

[222] L. Huang, Y. Li, H. Xu, Y. Xu, J. Xia, K. Wang, H. Li, X. Cheng, Synthesis and characterization of CeO_2/g-C_3N_4 composites with enhanced visible-light photocatalytic activity, Rsc Adv. 3 (2013) 22269–22279.

[223] T. Wu, G. Liu, J. Zhao, H. Hidaka, N. Serpone, Photoassisted degradation of dye pollutants. V. Self-photosensitized oxidative transformation of Rhodamine B under visible light irradiation in aqueous TiO_2 dispersions, J. Phys. Chem. B. 102 (1998) 5845–5851, https://doi.org/10.1021/jp980922c.

[224] L. Huang, H. Xu, R. Zhang, X. Cheng, J. Xia, Y. Xu, H. Li, Synthesis and characterization of g-C_3N_4/MoO_3 photocatalyst with improved visible-light photoactivity, Appl. Surf. Sci. 283 (2013) 25–32.

[225] L. Huang, F. Zhang, Y. Li, H. Wang, Q. Wang, C. Wang, H. Xu, H. Li, Chemical reduction implanted oxygen vacancy on the surface of 1D MoO_{3-x}/g-C_3N_4 composite for boosted LED light-driven photoactivity, J. Mater. Sci. 54 (2019) 5343–5358.

[226] S.C. Yan, S.B. Lv, Z.S. Li, Z.G. Zou, Organic–inorganic composite photocatalyst of g-C_3N_4 and TaON with improved visible light photocatalytic activities, Dalton Trans. 39 (2010) 1488–1491, https://doi.org/10.1039/B914110C.

[227] S. H. Elder, F. M. Cot, Y. Su, S. M. Heald, A. M. Tyryshkin, M. K. Bowman, Y. Gao, A.G. Joly, M. L. Balmer, Ana C. Kolwaite, and K. A. Magrini, D.M. Blake, The discovery and study of nanocrystalline TiO_2-(MoO_3) core−shell materials, ACS Publ. (2000). https://doi.org/10.1021/ja992768t.

[228] X. Zhou, B. Jin, R. Chen, F. Peng, Y. Fang, Synthesis of porous Fe_3O_4/g-C_3N_4 nanospheres as highly efficient and recyclable photocatalysts, Mater. Res. Bull. 48 (2013) 1447–1452.

[229] S. Kumar, B. Kumar, T. Surendar, V. Shanker, g-C_3N_4/$NaTaO_3$ organic–inorganic hybrid nanocomposite: high-performance and recyclable visible light driven photocatalyst, Mater. Res. Bull. 49 (2014) 310–318.

[230] Q. Wang, C. Chen, S. Zhu, X. Ni, Z. Li, Acetylene black quantum dots as a bridge for few-layer g-C_3N_4/MoS_2 nanosheet architecture: 0D–2D heterojunction as an efficient visible-light-driven photocatalyst, Res. Chem. Intermed. 45 (2019) 4975–4993.

[231] J. Yu, J. Lei, L. Wang, C. Guillard, J. Zhang, Y. Liu, M. Anpo, g-C_3N_4 quantum dots-modified mesoporous TiO_2–SiO_2 for enhanced photocatalysis, Res. Chem. Intermed. 45 (2019) 4237–4247.

[232] J. Lei, B. Chen, W. Lv, L. Zhou, L. Wang, Y. Liu, J. Zhang, An inverse opal TiO_2/g-C_3N_4 composite with a heterojunction for enhanced visible light-driven photocatalytic activity, Dalton Trans. 48 (2019) 3486–3495.

[233] L. Zhou, Y. Tian, J. Lei, L. Wang, Y. Liu, J. Zhang, Self-modification of g-C_3N_4 with its quantum dots for enhanced photocatalytic activity, Catal Sci. Technol. 8 (2018) 2617–2623.

[234] Y. Chen, Q. Dong, L. Wang, X. Guo, S. Ai, H. Ding, Graphitic-C_3N_4 quantum dots decorated {001}-faceted TiO_2 nanosheets as a 0D/2D composite with enhanced solar photocatalytic activity, Res. Chem. Intermed. 44 (2018) 7369–7389.

[235] Y. Liang, N. Sun, C. Zang, F. Chen, 1, 3, 5-Benzenetriyl substituted g-C_3N_4 for enhanced visible light photocatalytic activity, Res. Chem. Intermed. 45 (2019) 3641–3654.

[236] J. Li, L. Du, S. Jia, G. Sui, Y. Zhang, Y. Zhuang, B. Li, Z. Xing, Synthesis and photocatalytic properties of visible-light-responsive, three-dimensional, flower-like La–TiO_2/g-C_3N_4 heterojunction composites, RSC Adv. 8 (2018) 29645–29653.

[237] S.-H. Shin, W.-K. Jo, Longitudinal variations in indoor VOC concentrations after moving into new apartments and indoor source characterization, Environ. Sci. Pollut. Res. 20 (2013) 3696–3707.

[238] O. Fontelles-Carceller, M.J. Muñoz-Batista, M. Fernández-García, A. Kubacka, Interface effects in sunlight-driven Ag/g-C_3N_4 composite catalysts: study of the toluene photodegradation quantum efficiency, ACS Appl. Mater. Interfaces. 8 (2016) 2617–2627.

[239] M.J. Munoz-Batista, O. Fontelles-Carceller, A. Kubacka, M. Fernández-García, Effect of exfoliation and surface deposition of MnO_x species in g-C_3N_4: toluene photo-degradation under UV and visible light, Appl. Catal. B Environ. 203 (2017) 663–672.

[240] M.J. Muñoz-Batista, A. Kubacka, M. Fernández-García, Effect of g-C_3N_4 loading on TiO_2-based photocatalysts: UV and visible degradation of toluene, Catal Sci. Technol. 4 (2014) 2006–2015.

[241] Y. Shen, Z. Zhu, X. Wang, A. khan, J. Gong, Y. Zhang, Synthesis of Z-scheme g-C_3N_4/Ag/Ag_3PO_4 composite for enhanced photocatalytic degradation of phenol and selective oxidation of gaseous isopropanol, Mater. Res. Bull. 107 (2018) 407–415. https://doi.org/10.1016/j.materresbull.2018.08.017.

[242] H.-T. Ren, S.-Y. Jia, Y. Wu, S.-H. Wu, T.-H. Zhang, X. Han, Improved photochemical reactivities of $Ag_2O/g\text{-}C_3N_4$ in phenol degradation under UV and visible light, Ind. Eng. Chem. Res. 53 (2014) 17645–17653.
[243] L. Zhou, L. Wang, J. Lei, Y. Liu, J. Zhang, Fabrication of $TiO_2/Co\text{-}g\text{-}C_3N_4$ heterojunction catalyst and its photocatalytic performance, Catal. Commun. 89 (2017) 125–128, https://doi.org/10.1016/j.catcom.2016.09.022.
[244] K. Li, Y. He, P. Chen, H. Wang, J. Sheng, W. Cui, G. Leng, Y. Chu, Z. Wang, F. Dong, Theoretical design and experimental investigation on highly selective Pd particles decorated C_3N_4 for safe photocatalytic NO purification, J. Hazard. Mater. 392 (2020), 122357.
[245] W. Cui, L. Chen, J. Sheng, J. Li, H. Wang, Y. Zhou, Y. Sun, F. Dong, The pivotal roles of spatially separated charge localization centers on the molecules activation and photocatalysis mechanism, Appl. Catal. B Environ. 262 (2020), 118251.
[246] X. Ding, W. Ho, J. Shang, L. Zhang, Self doping promoted photocatalytic removal of no under visible light with Bi_2MoO_6: Indispensable role of superoxide ions, Appl. Catal. B Environ. 182 (2016) 316–325.
[247] J. Liao, W. Cui, J. Li, J. Sheng, H. Wang, P. Chen, G. Jiang, Z. Wang, F. Dong, Nitrogen defect structure and NO^+ intermediate promoted photocatalytic NO removal on H_2 treated $g\text{-}C_3N_4$, Chem. Eng. J. 379 (2020), 122282.
[248] K. Li, W. Cui, J. Li, Y. Sun, Y. Chu, G. Jiang, Y. Zhou, Y. Zhang, F. Dong, Tuning the reaction pathway of photocatalytic NO oxidation process to control the secondary pollution on monodisperse Au nanoparticles@$g\text{-}C_3N_4$, Chem. Eng. J. 378 (2019), 122184.
[249] J. Li, Y. Sun, G. Jiang, Y. Chu, S. Lee, F. Dong, Tailoring the rate-determining step in photocatalysis via localized excess electrons for efficient and safe air cleaning, Appl. Catal. B Environ. 239 (2018) 187–195.
[250] M. Ran, P. Chen, J. Li, W. Cui, J. Li, Y. He, J. Sheng, Y. Sun, F. Dong, Promoted reactants activation and charge separation leading to efficient photocatalytic activity on phosphate/potassium co-functionalized carbon nitride, Chin. Chem. Lett. 30 (2019) 875–880.
[251] H. Li, Y. Jing, X. Ma, T. Liu, L. Yang, B. Liu, S. Yin, Y. Wei, Y. Wang, Construction of a well-dispersed Ag/graphene-like $g\text{-}C_3N_4$ photocatalyst and enhanced visible light photocatalytic activity, RSC Adv. 7 (2017) 8688–8693, https://doi.org/10.1039/C6RA26498K.
[252] Q. Li, N. Zhang, Y. Yang, G. Wang, D.H.L. Ng, High efficiency photocatalysis for pollutant degradation with MoS_2/C_3N_4 heterostructures, Langmuir 30 (2014) 8965–8972, https://doi.org/10.1021/la502033t.
[253] S. Zhang, J. Li, M. Zeng, G. Zhao, J. Xu, W. Hu, X. Wang, In situ synthesis of water-soluble magnetic graphitic carbon nitride photocatalyst and its synergistic catalytic performance, ACS Appl. Mater. Interfaces. 5 (2013) 12735–12743, https://doi.org/10.1021/am404123z.
[254] Q. Liu, Y. Guo, Z. Chen, Z. Zhang, X. Fang, Constructing a novel ternary Fe(III)/graphene/$g\text{-}C_3N_4$ composite photocatalyst with enhanced visible-light driven photocatalytic activity via interfacial charge transfer effect, Appl. Catal. B Environ. 183 (2016) 231–241, https://doi.org/10.1016/j.apcatb.2015.10.054.
[255] X. Bai, R. Zong, C. Li, D. Liu, Y. Liu, Y. Zhu, Enhancement of visible photocatalytic activity via Ag@C_3N_4 core–shell plasmonic composite, Appl. Catal. B Environ. 147 (2014) 82–91, https://doi.org/10.1016/j.apcatb.2013.08.007.
[256] F. He, G. Chen, Y. Zhou, Y. Yu, L. Li, S. Hao, B. Liu, ZIF-8 derived carbon (C-ZIF) as a bifunctional electron acceptor and HER cocatalyst for $g\text{-}C_3N_4$: construction of a metal-free, all carbon-based photocatalytic system for efficient hydrogen evolution, J. Mater. Chem. A. 4 (2016) 3822–3827, https://doi.org/10.1039/C6TA00497K.
[257] J. Li, Z. Zhang, W. Cui, H. Wang, W. Cen, G. Johnson, G. Jiang, S. Zhang, F. Dong, The spatially oriented charge flow and photocatalysis mechanism on internal van der Waals heterostructures enhanced $g\text{-}C_3N_4$, ACS Catal. 8 (2018) 8376–8385.
[258] B. Chen, L. Zhou, Y. Tian, J. Yu, J. Lei, L. Wang, Y. Liu, J. Zhang, Z-scheme inverse opal CN/BiOBr photocatalysts for highly efficient degradation of antibiotics, Phys. Chem. Chem. Phys. 21 (2019) 12818–12825.
[259] L. Zhou, Z. Liu, Z. Guan, B. Tian, L. Wang, Y. Zhou, Y. Zhou, J. Lei, J. Zhang, Y. Liu, 0D/2D plasmonic $Cu_{2-x}S/g\text{-}C_3N_4$ nanosheets harnessing UV-vis-NIR broad spectrum for photocatalytic degradation of antibiotic pollutant, Appl. Catal. B Environ. 263 (2020), 118326.
[260] Y. Wu, Y. Zhang, Y. Gong, L. Niu, C. Li, X. Liu, Rubidium Chloride (RbCl)-assisted defective $g\text{-}C_3N_4/Bi_2O_2CO_3$ layered heterostructure photocatalyst for enhanced charge separation and photodecomposing antibiotics, Nanosci. Nanotechnol. Lett. 11 (2019) 1093–1103.